

# Density-Dependent Liquid Nitromethane Decomposition: Molecular Dynamics Simulations Based on ReaxFF

Naomi Rom,<sup>\*,†</sup> Sergey V. Zybin,<sup>‡</sup> Adri C. T. van Duin,<sup>§</sup> William A. Goddard, III,<sup>‡</sup> Yehuda Zeiri,<sup>||,⊥</sup> Gil Katz,<sup>†</sup> and Ronnie Kosloff<sup>†</sup>

<sup>†</sup>Fritz Haber Research Center for Molecular Dynamics, Hebrew University, Jerusalem 91904, Israel

<sup>‡</sup>Materials and Process Simulation Center, 139-74, California Institute of Technology, Pasadena, California 91125, United States

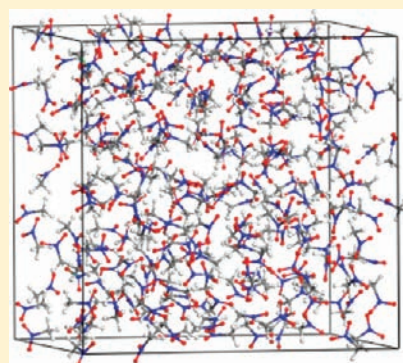
<sup>§</sup>Department of Mechanical and Nuclear Engineering, Pennsylvania State University, University Park, Pennsylvania 16802, United States

<sup>||</sup>Bio-medical Engineering, Ben Gurion University, Beer-Sheva 84105, Israel

<sup>⊥</sup>Division of Chemistry, NRCN, P.O. Box 9001, Beer-Sheva 84190, Israel

**S** Supporting Information

**ABSTRACT:** The decomposition mechanism of hot liquid nitromethane at various compressions was studied using reactive force field (ReaxFF) molecular dynamics simulations. A competition between two different initial thermal decomposition schemes is observed, depending on compression. At low densities, unimolecular C–N bond cleavage is the dominant route, producing CH<sub>3</sub> and NO<sub>2</sub> fragments. As density and pressure rise approaching the Chapman–Jouget detonation conditions (~30% compression, >2500 K) the dominant mechanism switches to the formation of the CH<sub>3</sub>NO fragment via H-transfer and/or N–O bond rupture. The change in the decomposition mechanism of hot liquid NM leads to a different kinetic and energetic behavior, as well as products distribution. The calculated density dependence of the enthalpy change correlates with the change in initial decomposition reaction mechanism. It can be used as a convenient and useful global parameter for the detection of reaction dynamics. Atomic averaged local diffusion coefficients are shown to be sensitive to the reactions dynamics, and can be used to distinguish between time periods where chemical reactions occur and diffusion-dominated, nonreactive time periods.



chemical reactions occur and diffusion-

## 1. INTRODUCTION

Nitromethane (CH<sub>3</sub>NO<sub>2</sub>, NM), a high explosive (HE), has been studied intensively both experimentally<sup>1–5</sup> and theoretically.<sup>3,6–10</sup> Either a liquid phase or a crystal phase was employed as the initial state. The present study focuses on reactive molecular dynamics (MD) simulations of NM in the hot and dense liquid phase. The main goal of this study is to identify and quantify the detailed chemical reactions that occur during detonation. These reactions begin with the first molecular decomposition steps followed by the formation of final products. The calculations were performed under various temperature and compression conditions. These conditions simulate rapid laser heating experiments in diamond anvil cells, where the sample volume is held constant. The purpose of the present study is to obtain insight on the reaction mechanisms governing the initiation and detonation processes. The temperatures and compressions range examined include the typical conditions at the detonation wavefront.

A sample of the possible NM unimolecular decomposition pathways suggested<sup>11</sup> are

- CH<sub>3</sub>NO<sub>2</sub> → CH<sub>3</sub> + NO<sub>2</sub>
- CH<sub>3</sub>NO<sub>2</sub> → CH<sub>3</sub>ONO → CH<sub>2</sub>O + HNO
- CH<sub>3</sub>NO<sub>2</sub> → CH<sub>3</sub>NO + O

- CH<sub>3</sub>NO<sub>2</sub> → CH<sub>3</sub>O + NO
- CH<sub>3</sub>NO ↔ CH<sub>2</sub>NOH
- CH<sub>3</sub>NO<sub>2</sub> → CH<sub>2</sub>NOOH

In a previous study,<sup>8</sup> the decomposition of solid NM was calculated using MD simulations with on-the-fly calculations of molecular forces with density functional theory. In these simulations, dense solid NM (1.97 g/cm<sup>3</sup> and 2.2 g/cm<sup>3</sup>) was rapidly heated to 3000 K and 4000 K. The first step revealed in the thermal decomposition was *intermolecular* proton transfer forming [H<sub>3</sub>CNO<sub>2</sub>H]<sup>+</sup> and aci ion [H<sub>2</sub>CNO<sub>2</sub>]<sup>−</sup>. The second step observed was *intramolecular* proton transfer forming aci acid [H<sub>2</sub>CNO<sub>2</sub>H]. Then, additional fragments were formed, such as CH<sub>2</sub>NO<sup>+</sup>, OH<sup>−</sup>, and H<sub>2</sub>O. These reaction products were related to condensed phase reactions, whereas the C–N bond break, being the weakest in the molecule (*D*<sub>0</sub> = 60.1 kcal/mol in the gas phase<sup>23</sup>), prevails in gas phase or dilute fluid decomposition.

The hypothesis that hydrogen abduction is the rate-determining step at a pressure of 10 kbar and at a temperature of 273 °C, is

**Received:** March 3, 2011

**Revised:** July 20, 2011

**Published:** August 03, 2011

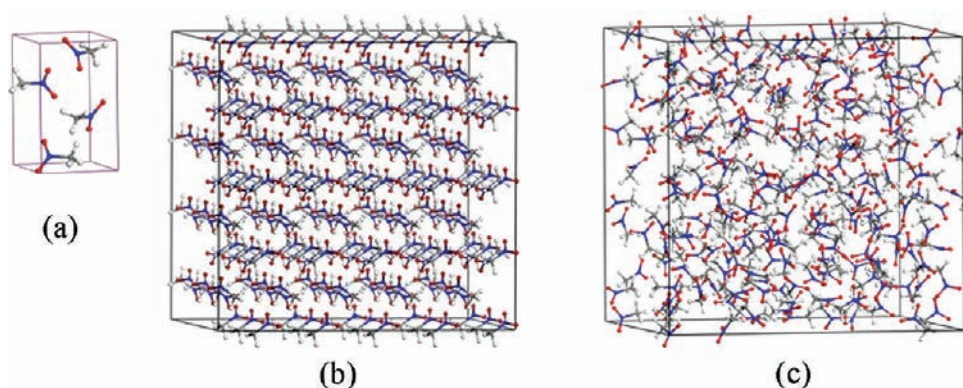


**Figure 1.** NM Crystal. (a) unitcell (b)  $5 \times 4 \times 3$  energy minimized supercell, and (c) liquid NM supercell at ambient conditions.

supported by the measured time to detonation with deuterated NM, which was found to be 10 times longer than with protonated NM.<sup>1</sup> However, interpolation to higher temperatures suggests that above 330 °C the time to denotation of NM is longer than that of deuterated NM. Thus, possibly H-transfer is more important at similar compressions and lower temperatures (<330 °C).

In ref 5, the effect of pressure (<7 GPa) on the thermal decomposition of NM was studied in diamond anvil cell experiments where the samples were heated up to 450 K. It was found that both pressure and temperature accelerate the rate of thermal decomposition, supporting a bimolecular decomposition mechanism. The suggested rate-controlling leading reaction, supported by QM calculation, is



with calculated activation energy of 32.5 kcal/mol.

In the present work, we apply a MD approach based on the reactive force field ReaxFF to study the decomposition of liquid NM at a wide range of compression values ( $0.56 \leq V/V_0 \leq 1$ , where  $V$  is the volume after compression and  $V_0$  is the calculated ambient conditions volume) and temperatures (2500–4500 K). Three regimes of the reaction are identified and analyzed independently: initiation step, intermediate reactions, and stable products creation. We found that the mechanism of the initial rate-determining step in NM decomposition depends strongly on its density ( $\rho$ ): At ambient density and below 30% compression, C–N bond cleavage is the first event, as in the gas phase. At higher densities, in the vicinity of the Chapman–Jouget (CJ) state (stationary detonation, fully reacted HE, products in chemical equilibrium),  $\text{CH}_3\text{NO}$  is the dominant initial decomposition product. The former process is unimolecular whereas the latter fragment is formed by various mechanisms.

Thermal rate constants were evaluated for the initial endothermic decomposition stage for different initial densities. After some delay (temperature and pressure dependent), various intermediate reactions commence, including autocatalytic ones where NM reacts with its fragments. These reactions are presented in detail in section 3.4. The evolution of final products ( $\text{H}_2\text{O}$ ,  $\text{CO}_2$ ,  $\text{N}_2$ ,  $\text{H}_2$ ,  $\text{CO}$ ,  $\text{NH}_3$ , and  $\text{OH}$ ) begins in the intermediate stage and terminates when they reach stable amounts, as shown in section 3.5.

The paper is organized as follows: In section 2 the computational approach is described both for the simulations and kinetic analysis. Simulation results and analysis (fragments, rate constants, exothermicity, enthalpy) are presented in section 3, and conclusions are summarized in section 4. Supplementary data (potential parameters and bond order cut off values) are given in the Supporting Information.

## 2. COMPUTATIONAL APPROACH

The parallel version of the ReaxFF-MD code,<sup>12,13</sup> GRASP (General Reactive Atomistic Simulation Package) was employed to study the behavior of liquid NM under various conditions. ReaxFF-MD was used in various applications, such as surface catalysis<sup>14</sup> and combustion chemistry.<sup>15</sup> In addition, it was used to study the initial chemical reactions that occur during thermal or shock-induced decomposition of HE materials (e.g., NM,<sup>9</sup> cyclotrimethylenetrinitramine (RDX),<sup>16,17</sup> and triacetone triperoxide (TATP)<sup>18</sup>), and recently in the calculation of directional anisotropy in pentaerythritoltetranitrate (PETN) single crystals resulting from combined shear and compressive loading.<sup>19</sup> Note that ReaxFF potentials were trained for ground-state processes only, thus fragments obtained in these simulations are radicals or stable molecules (not ionic species). ReaxFF parameters were fitted to results of multiple ab initio quantum mechanical (QM) calculations. ReaxFF-MD simulations were shown to reproduce the QM results with high accuracy. Some examples<sup>20</sup> are bonds dissociation (gas phase reactions path), compression curves, geometry distortions (angles and torsion), charges, IR-spectra, condensed phase structures, and equations of state of molecules and crystals with H, C, N and O atoms.

Below we describe the procedure employed to prepare the liquid samples at various compressions followed by the conditions used in the heat-up simulations.

**2.1. Sample Preparation.** Preparation of liquid NM starts with a solid slab in which the NM molecules are arranged according to their crystal structure. The molecular slab (supercell) is obtained by multiplying solid NM unit cell (orthorhombic cell, Figure 1a, with  $a, b, c = 5.228, 6.293, 8.664$  Å, respectively) by an integer along the different directions. Here,  $5 \times 4 \times 3$  expansion along  $x, y,$  and  $z$  directions was employed. Hence, the total number of molecules in the simulation was 240 (1680 atoms). Energy minimization is carried out to obtain optimized equilibrium geometry of the expanded crystal (Figure 1b).

**2.1.1. Liquid Creation (Ambient Conditions).** In order to obtain a liquid structure at ambient conditions, the following procedure was applied to the relaxed crystal supercell:

- The cell volume was increased by 50%, then its energy was minimized resulting in an optimized geometry (simulation length – 0.25 ps).
- The obtained supercell was heated to 400 K (10 ps), well above the NM melting point (244 K).
- The hot cell was heavily compressed (NPT simulation at 1 GPa and 400 K, 30 ps).

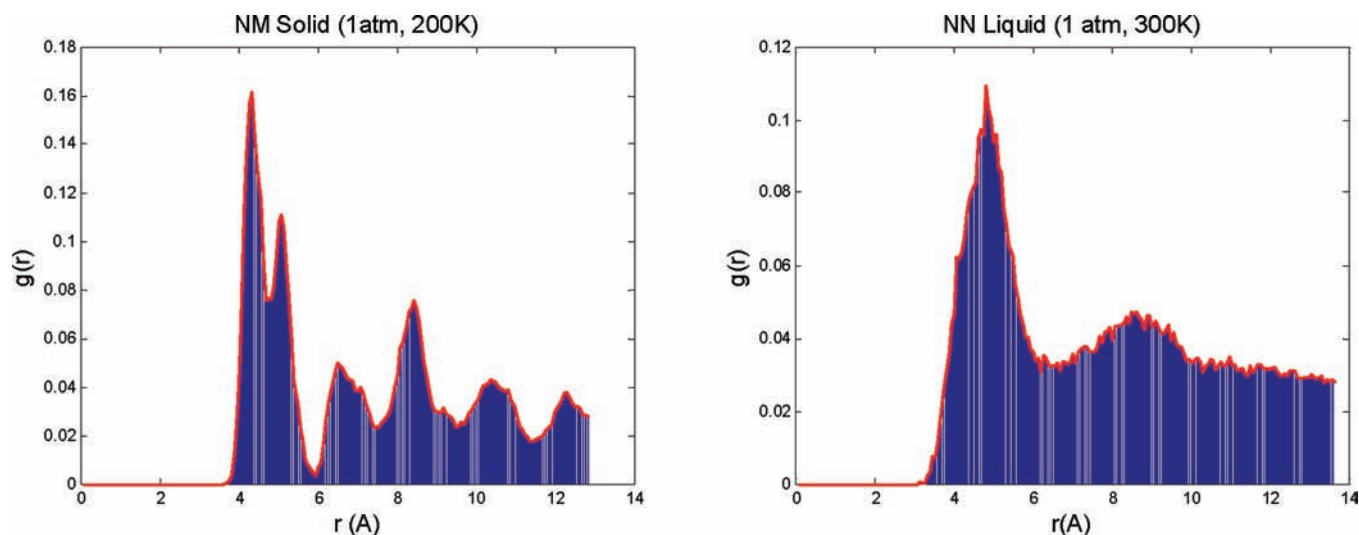


Figure 2. Radial distribution function for NM molecules in the solid (left) and liquid (right) phases. Distance units are Å.

- Cooling and decompression was applied (NPT at 1 atm and 300K, 30 ps). Calculated mass density of the liquefied sample at the end of the simulation was  $1.111 \text{ gr/cm}^3$  ( $a, b, c = 28.327, 27.386, 28.222 \text{ Å}$ , respectively). It differs only by  $\sim 2\%$  from the measured density  $1.137 \text{ gr/cm}^3$ .
- The liquid cell was thermalized (NVT,  $T = 300\text{K}$ , 2 ps), and pressure oscillations reduced to  $\pm 0.5 \text{ GPa}$ .
- Finally the system state was relaxed (NVE simulation, 1 ps). A typical liquid supercell is shown in Figure 1c.

The time step in all the calculations described above was 0.25 fs. In the simulations, a simple rescaling thermostat was used, with temperature correction proportional to half the difference between the target and current temperature.

Radial distribution functions for the solid and liquid simulation cells are presented in Figure 2. Here,  $r$  is the distance between two NM molecules. As expected, typical structured behavior and smooth modulations are obtained for the solid and liquid cells, respectively. Results are shown for  $r \leq d/2$ , where  $d$  is the smallest cell vector.

**2.2. Liquid Compression ( $T = 300 \text{ K}$ ,  $P = 1 \text{ atm}$ ).** In order to obtain liquid in various compressions, we began with the liquid sample prepared by the process described above and volumetrically compressed it by the desired amount. Then, it was energy-minimized for 0.5–1 ps, depending on the magnitude of the compression, until equilibrium atomic positions were obtained. Finally, each sample was thermalized using NVT simulation at 300 K (2 ps), using a velocity rescaling thermostat. It is important to note that none of the NM molecules decomposed during these stages.

**2.3. Heat-Up Simulations.** Heat-up simulations of liquid NM were made in two stages: Initially, the sample at a fixed density was heated rapidly (within 100 fs, using time step 0.25 fs) from room temperature to the desired final temperature ( $T_f$ ). Then, NVT simulations were carried out at  $T_f$  until the final products approached constant amounts. The rapid heating is carried out on a time scale similar to that of a detonation wave passing through the simulation cell ( $\sim 500 \text{ fs}$ ). The time step used in NVT simulations was 0.1 fs, and the simulations progressed for 60–80 ps.

Thermal rate constants were calculated at three regimes within the simulations:

- Initial decomposition reaction/s (endothermic).

- Intermediate reactions and products.
- Stable products formation with the main products:  $\text{H}_2\text{O}$ ,  $\text{CO}_2$ ,  $\text{N}_2$ ,  $\text{H}_2$ ,  $\text{CO}$ ,  $\text{NH}_3$  and  $\text{OH}$ .

The following section describes the methods employed for the chemical kinetics analysis.

**2.3.1. Chemical Reactions and Fragments Analysis.** Fragments analysis was done with “BondFrag”, a code developed in Goddard’s group at Caltech. For each pair of atoms in the simulation cell, a “bond order” is calculated. Then, according to cutoff values predefined for each pair (given in the Supporting Information), the code determines whether a chemical bond exists or not, thus fragments or molecules are being formed.

According to the reaction regimes mentioned above, fragments were examined in three stages: Creation of primary fragments, representing a reaction bottleneck at the very beginning of liquid NM decomposition; intermediate fragments formation, where many reactions occur simultaneously leading to multiple fragments (unstable and stable); and final products stabilization when thermodynamic equilibrium is reached. The main chemical reactions occurring in the initial stages of NM decomposition are listed below.

**2.3.2. Rate Constants Analysis.** Thermal rate constants were calculated as a function of density and temperature in the three different reaction stages. The average potential energy (PE) of the system was monitored during the simulation. It was found that PE exhibits a maximum close to the initial stages of the simulation. Fragments analysis (see section 3.4) reveals the nature of the peak: It roughly separates between the initial, endothermic decomposition of NM and the intermediate, multiple reactions stage. The time when the PE reaches a maximum,  $t_{\text{max}}$ , was determined for each simulation. This was accomplished by fitting a smooth function (sum of decreasing and increasing exponential functions) to the evolution of PE during the simulation and finding its maximum. In cases where the PE maximum was too close to the simulation initiation (namely, at high temperatures), a local polynomial fit was applied in the vicinity of the PE maximum to get  $t_{\text{max}}$  which was then used to distinguish between NM initial decomposition and the intermediate reactions stage.

For each simulation, rate constants in the three stages are deduced as follows:

- *Initial decomposition stage rate constant,  $k_1[\rho, T]$* : The hot liquid NM molecules decay was fitted with a first order decay expression,  $N(t)$ , from the beginning of the decomposition, at  $t_0$ , until  $t_{\max}$ :

$$N(t) = N_0 \cdot \exp[-k_1(t - t_0)] \quad (1)$$

Note that in previous works<sup>7,16</sup> this fit was made along the full NM decay, including the zone where intermediate reactions take place and hence influence the rate constant, introducing inaccuracy into the single exponential function fit.

- *Intermediate decomposition stage,  $k_2[\rho, T]$* : Bypassing the complexity of chemical reactions at this stage, an effective first order rate constant is obtained by fitting a decaying exponential function to the decaying part of PE curve,  $U(t)$ , starting from  $t_{\max}$ :

$$U(t) = U_{\infty} + \Delta U_{\text{exo}} \cdot \exp[-k_2(t - t_{\max})] \quad (2)$$

$U_{\infty}$  is the asymptotic value of PE (products) and  $\Delta U_{\text{exo}} = U(t_{\max}) - U_{\infty}$ . The latter is the exothermicity, or the heat release, in the NM decomposition reaction. This type of fitting was also used in the thermal decomposition study of RDX,<sup>16</sup> triaminotrinitrobenzene (TATB), and octahydro-1,3,5,7-tetranitro-1,3,5,7-tetrazocine (HMX).<sup>20</sup> NM decomposition enthalpy change,  $\Delta H$ , can be estimated from

$$\Delta H = -\Delta U_{\text{exo}} + V(P_{\infty} - P(t_{\max})) \quad (3)$$

As will be seen in section 3.6,  $\Delta H$  seems to be correlated with the initial decomposition mechanism of NM (which is pressure dependent). If so, it can serve as a simple yet sensitive tool in identifying mechanism changes under various conditions.

- *Final products evolution stage,  $k_3$* : Effective rate constants (due to the variety of reactions leading to their formation) for final products creation can be calculated by fitting the following function to each product's time evolution,  $C(t)$ :

$$C(t) = C_{\infty} \cdot (1 - \exp[-k_3(t - t_i)]) \quad (4)$$

$t_i$  is the product's time of formation. Note that this fitting needs to be made until each product reaches a stable amount, otherwise the fitted parameters will depend on the simulation length.  $C_{\infty}$  is the estimated asymptotic amount of the products, and can be compared to measurements<sup>22</sup> and results of thermochemical computations<sup>22</sup> (see section 3.5).

Following the evaluation of the temperature- and density-dependent rate constants in the initial and intermediate decomposition stages of liquid NM, a fit to the Arrhenius equation is made to obtain activation energies and pre-exponential factors as a function of density for these stages. Kinetic analysis results are presented in the following section.

**2.3.3. Diffusion Coefficient and Mean Square Displacement (MSD) of the Atoms.** The mobility of atoms during the simulation is influenced by the pressure and temperature, as well as by their participation in chemical reactions. Diffusion

**Table 1. Densities, Simulation Cell Volumes and Compressions Used in Heat-Up Simulations**

mass density [gr/cm <sup>3</sup> ]	cell volume, $V$ [cm <sup>3</sup> ]	Compression, $V/V_0$
1.111	21894	1
1.234	19704	0.9
1.389	17515	0.8
1.587	15325	0.7
1.852	13136	0.6
1.984	12260	0.56

coefficient,  $D$ , can be estimated using Einstein's expression:

$$D = \lim_{t \rightarrow \infty} \frac{1}{6N_m t} \left\langle \sum_{j=1}^{N_m} [r_j(t) - r_j(0)]^2 \right\rangle \quad (5)$$

$r_j(t)$  is the coordinate of atom  $j$  at time  $t$ .  $N_m$  is the number of atoms. In the case of chemically reactive simulations, the diffusion coefficient is not expected to be constant, but rather related to the reactions' evolution. In section 3.6, MSDs are calculated separately for each NM atom (C, H, N, O).

### 3. RESULTS

Heat-up simulations were carried out at a constant density. The desired temperature was attained by performing rapid heating for 100 fs, followed by a constant, final temperature simulation. Densities used are the calculated ambient mass density (1.111 gr/cm<sup>3</sup>) and a series of volumetric compressions (10, 20, 30, 40 and 44%; see Table 1). The temperatures vary in the range between 2500 K and 4500 K. The simulation with highest density at  $\sim 3000$  K is close to the CJ state of solid NM, which was studied in detail.<sup>8,9</sup> Note that in the latter studies 32 NM molecules were included in the simulations, whereas 240 molecules are used here. CJ pressure and particle velocity measured for liquid NM<sup>21</sup> (initial density 1.14 gr/cm<sup>3</sup>) are  $13.0 \pm 0.4$  GPa and  $1.8 \pm 0.05$  km/s, respectively, and the CJ detonation velocity is 6.3 km/s. Accordingly, the CJ density is  $1.596 \pm 0.02$  gr/cm<sup>3</sup>. In ref 25, the measured CJ pressure and detonation velocity are 12.71 GPa and 6.311 km/s, thus CJ density is 1.5805 gr/cm<sup>3</sup>. Note that the CJ density of liquid NM is at a density of approximately 30% compression (see Table 1).

**3.1. Liquid NM Initial Decay.** The time evolution of NM (normalized by the initial amount of 240 molecules) is presented in Figure 3, for the different temperature values. Each plot shows results for a different initial density. As expected, the decomposition rate increases with temperature increase.

The initial, rapid heating stage is not shown in these plots. In some cases, one or two NM molecules (<1%) decomposed via a C–N bond break. In the simulation with 20% compression at 4500 K five NM molecules reacted (2%) in this stage: Two molecules formed a van der Waals dimer, and two C–N bonds and one C–H bonds were fractured. In these cases, the initial reactions were sensitive to the time step used. However, in order to be consistent with the other simulations, we proceeded to the NVT simulation with the same time step as in the other cases (0.25 fs).

NM is an insensitive HE. Our simulations show that a relatively high temperature ( $\sim 2500$  K) is required for the decomposition process to commence at a pronounced rate. This

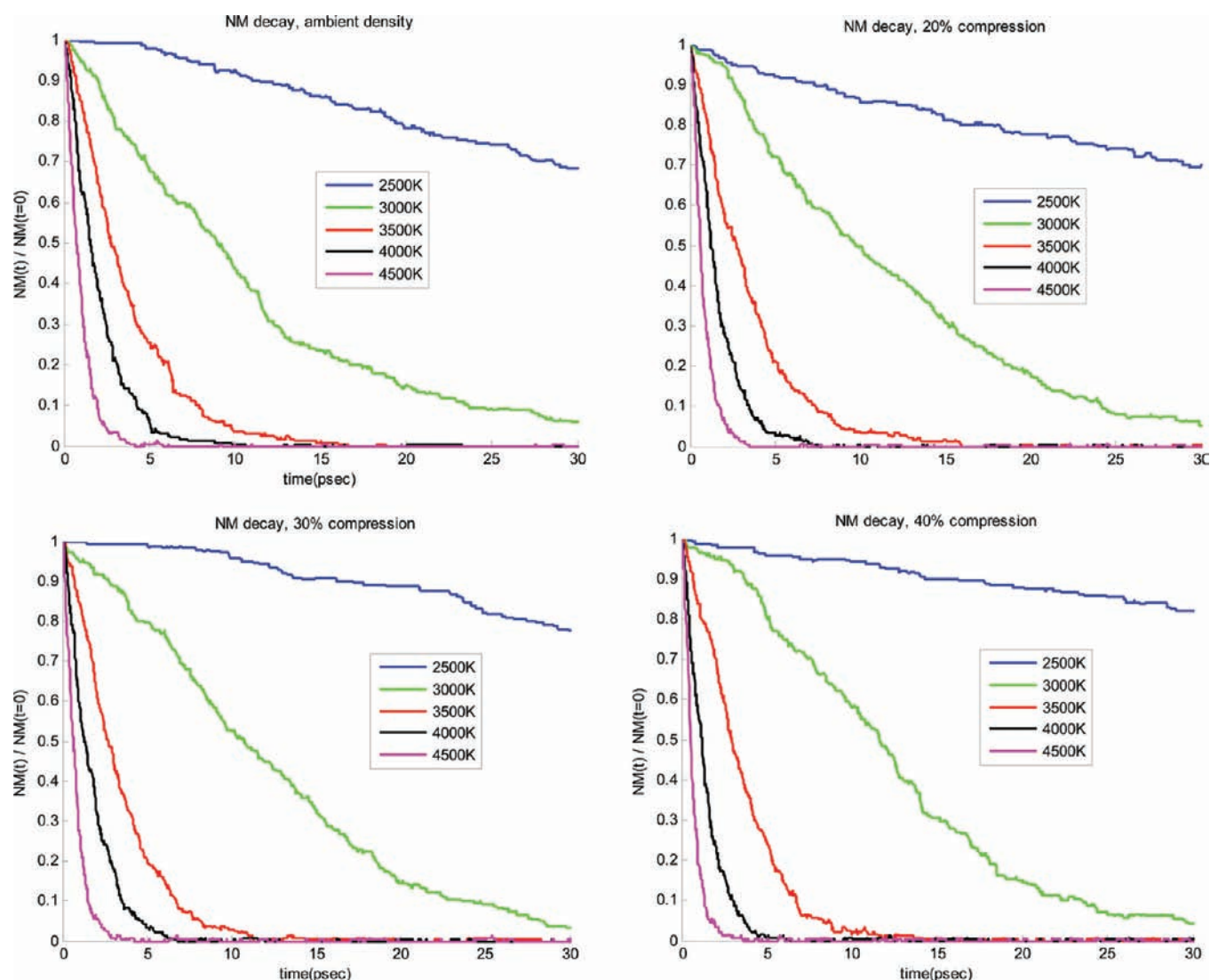


**Figure 3.** NM decay versus simulation time for various temperatures, plotted separately per density (ambient density, 20, 30, and 40% compressions).

suggests a correlation between the initial temperature in which HE starts to decompose and its sensitivity.

The density-dependent decomposition of NM is shown in Figure 4 for various temperatures. Above 2500 K, in most cases NM decomposition starts as soon as the NVT simulation begins. Two tendencies are seen in the initial decomposition stage of NM, depending on the temperature regime:

- At temperatures  $\leq 3500$  K, the decay rate of NM slows down as density is increased from ambient density to 40% compression. Further increase of density speeds up NM decay (see Figure 4).
- At temperatures  $\geq 4000$  K, the decay rate of NM generally increases with density/pressure increase.

These tendencies determine the characteristics of the initial decomposition stage rate constant,  $k_1$ , depending on pressure and temperature, as shown in section 3.3. In Figure 5, a comparison between the density-dependent decay rates at 2500 and 3500 K are presented by shifting the curves such that they coincide at a common decomposition value (3%). The tendency mentioned above for lower temperatures is seen.

Note that in the intermediate reactions regime ( $t > t_{\max}$ ), as decomposition progresses at lower temperatures ( $\leq 3500$  K), the NM decay slopes with 40% and 44% compressions get steeper and bypass lower compression ones (see marks on Figure 4). This increase in NM decay is correlated with the larger PE decay rates obtained at higher compressions (see Figure 6 and section 3.2).

We will further examine the nontrivial dependence of NM decay on pressure and temperature by analyzing the fragments production and chemical reactions (see section 3.4). At this point we note that in the bulk phase at lower temperatures, surrounding molecules act as a “thermal bath” that absorbs energy from excited molecules and cools them down. In the case of unimolecular decomposition, increasing the density strengthens the coupling of the excited vibrational mode to the bath, and the molecule’s decomposition rate is reduced. On the other hand, with bimolecular reactions, increasing the density reduces intermolecular spacing and increases the reaction rate. Hence, increasing the density has a reversed effect on the different types of reaction mechanisms at lower temperatures ( $\leq 3500$  K here). As will be seen below, the reversed tendency of the initial NM decay

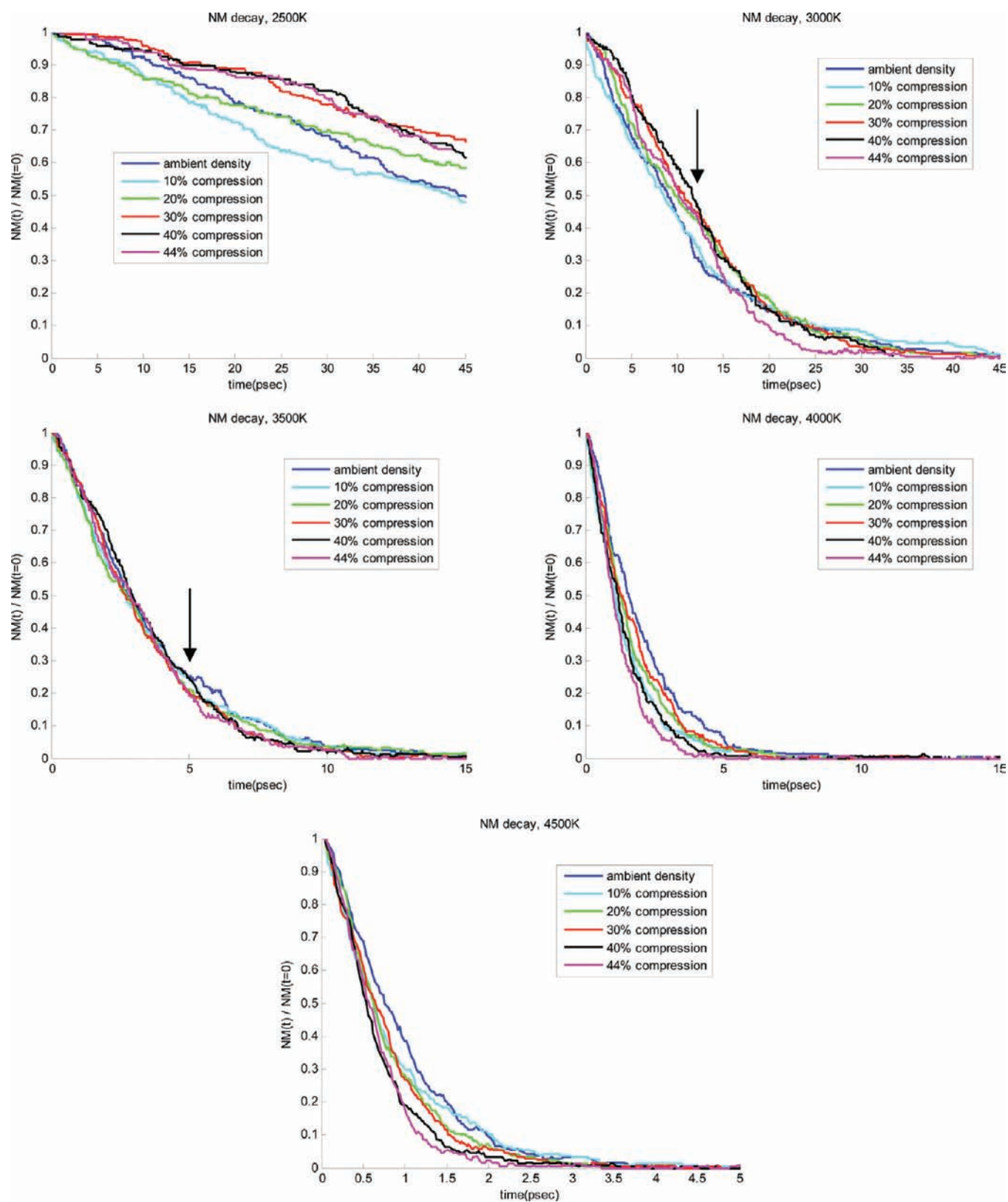


**Figure 4.** NM decay versus simulation time for various densities, plotted separately per temperature (between 2500 and 4500 K). Note different scales per plot. The arrows mark the time where NM decomposition speeds up for 40% and 44% compressions at 3000 K.

rate as a function of density is related to a transition from a dominant unimolecular decomposition reaction at lower

densities, to a bimolecular path that becomes preferable, in comparison to the unimolecular one, at very high compressions.

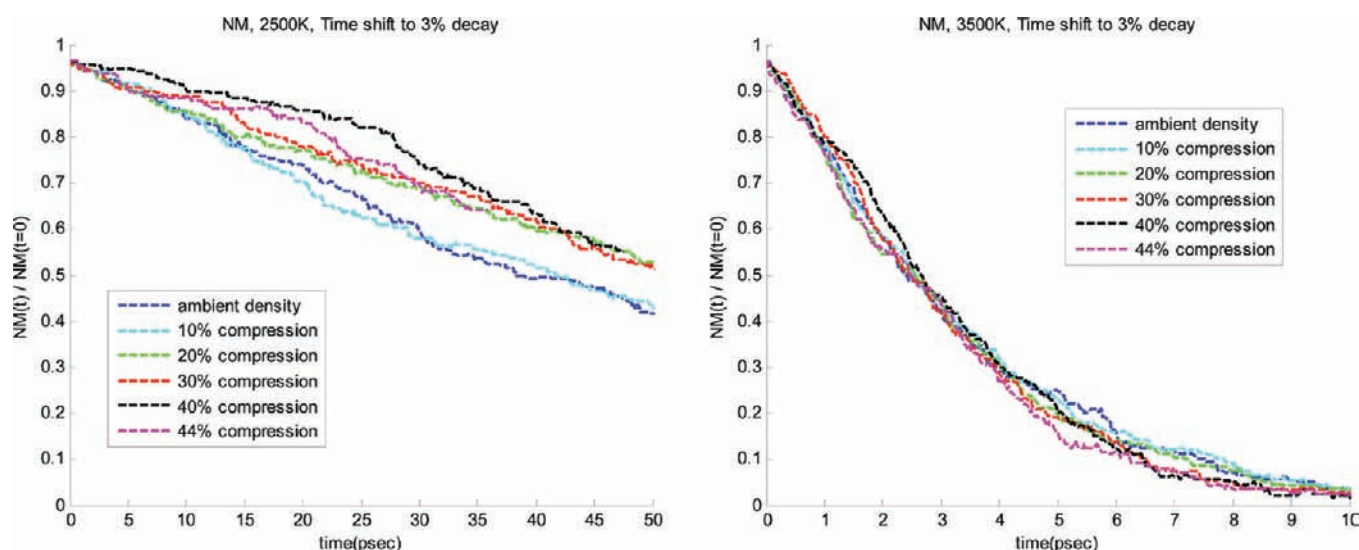


**Figure 5.** NM decay at 2500 and 3500 K for various densities, plotted versus shifted simulation time such that decomposition at all densities coincides at 3%.

However, at temperatures  $\geq 4000$  K, increasing the density enhances the decomposition rate monotonically. The NM molecules are highly excited, decomposition reactions occur very fast, and cooling by thermal bath is ineffective.

**3.2. Pressure and PE Evolution.** The time evolution of the total pressure and PE as a function of density (see Table 1) is presented in Figure 6. Results for each constant temperature are shown separately. Note that the rapid heating stage is not presented. Moving average was applied to the pressure presented in the plots to reduce numeric noise.

Generally, the pressure initially decreases, then in the vicinity of the time where PE is maximal ( $t_{\max}$ ) it starts to increase gradually toward an asymptotic value, which marks chemical equilibrium. As expected, the pressure rises with density and temperature.

Under all conditions studied, first the PE increases then it exponentially decreases until some asymptotic value is reached. The initial behavior is related to the existence of endothermic reactions in the beginning of NM decomposition (or detonation) process. It is followed by a second stage, where various intermediate reactions take place, some of which involve NM molecules, while in others NM decomposition products participate. The third and last stage marks the termination of chemical reactions with the formation of thermodynamically stable final products that reach a saturation value. Chemical rate constants can be calculated for each of these three regions, as discussed below. The NM decomposition exothermicity (i.e., the heat released in the reactions) is calculated from the difference between the PE maximum and its asymptotic value as well as the pressure change (see section 3.6).

The PE variation with time for temperatures  $\geq 3000$  K can be divided into two types, depending on the density: In the PE exponential decay region, samples with compression below 30% have slower decay rates, while those with higher compressions decay at a similar, faster rate (see Figure 6 and extended time PE behavior for 3000 K in Figure 7). As mentioned in the previous section, the PE decay rate is related to the NM decay rate at  $t > t_{\max}$ . Note that the PE decay rate analysis in section 3.3 shows the general attitude of decay rate increase with compression (and temperature).

Finally, the asymptotic value of PE increases with density and temperature.

**3.3. Decomposition Reactions Rate Constants:  $k_1$  and  $k_2$ .** Rate constants for the initial and intermediate decomposition stages were calculated with the fitting procedure used in ref 1 (also partly in ref 16) and briefly described above (see section 2.3.2). The analysis starts in finding the time where PE reaches its maximal value,  $t_{\max}$ . These times are shown in Table 2 for the various densities and temperatures studied, and are plotted in Figure 8. An example of the fitting used for  $t_{\max}$  evaluation and PE decay rate ( $k_2$ ) is shown for 3500 K at ambient density and 30% compression in Figure 9.

Two general observations can be made on the character of secondary reactions initiation ( $t_{\max}$ ):

- The higher the temperature, the smaller is  $t_{\max}$  (secondary reactions start sooner, the barrier is overcome more easily).
- As pressure/density increases,  $t_{\max}$  decreases.

The latter can be understood when the reactions involved have more than one reactant. As mentioned above, such reactions are facilitated by pressure and density increase, due to the reduction in intermolecular spacing. This is characteristic of reactions at a time beyond  $t_{\max}$  and also for initial decomposition reactions of NM at 30% compression and higher. Both cases will be discussed further in the fragments analysis section 3.4. There are some exceptions to the mentioned density-dependent tendency of  $t_{\max}$  due to inaccuracy in its determination when PE curves have a “flat top”, as is the case for  $T \leq 3000$  K for all densities, and for 3500 K for densities  $\geq 30\%$  compression (see Figure 6). Longer simulations (hundreds of picoseconds) are required to better characterize the evolution of intermediate reactions and products at these conditions.

For the PE fit ( $k_2$ ), we used temperatures  $\geq 3500$  K only, since as mentioned, the reaction progress at lower temperatures is relatively slow, and the decay cannot be fitted by a single exponential function (at least within the time regime used in the present simulations).

NM decay rates,  $k_1[\rho, T]$ , were obtained using eq 1 in the time range  $[t_0, t_{\max}]$ . Examples of NM decay curve fitting are given in Figure 10 for ambient density and 30% compression at 3000 and

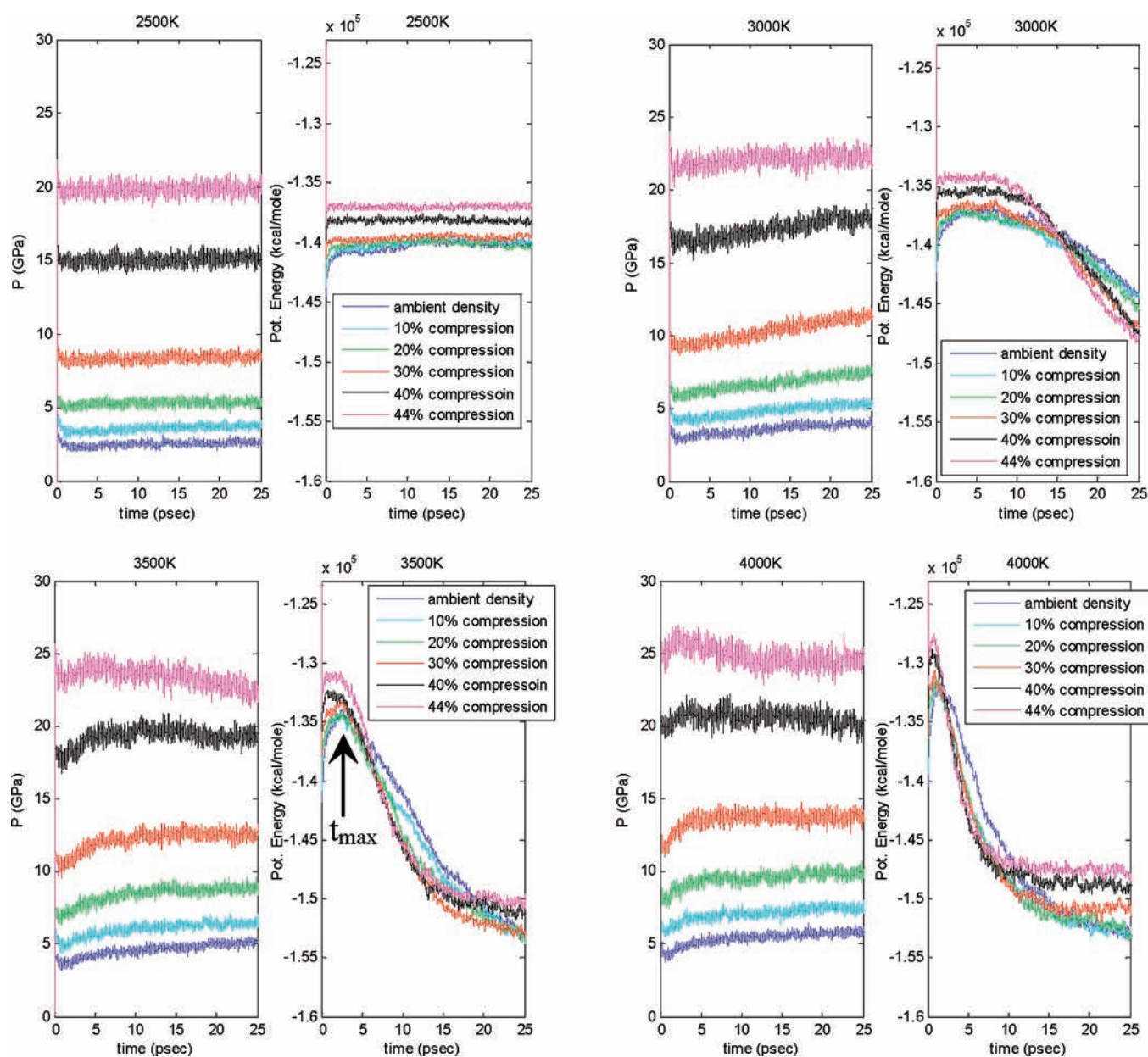


**Figure 6.** Pressure (left) and PE (right) versus simulation time for various densities, plotted separately per constant temperature simulation (2500–4000 K). Energy units are kcal/mole, where “mole” here refers to a mole of simulation cells. In order to change energy units to kcal/mole of NM molecules, the values in the plots should be divided by 240 (number of molecules/cell).

4000 K. Also shown is a single exponential function fit throughout the whole simulation period, as used, for instance, in ref 7. As can be seen, at the lower temperature and density, as well as in the high temperature and both densities, a single exponential function fit throughout the simulation is fairly good. However, for higher density at 3000 K a single exponent does not fit the NM decay curve well, with a large deviation in the initial reactions region. As will be seen in the next section, at high compressions bimolecular (or higher) mechanisms compete with the initial unimolecular decomposition, causing the large deviation from an overall single exponential function behavior.

Arrhenius plots of the rate constants for the initial and secondary decomposition stages of NM are shown in Figure 11. The behavior of  $k_2$  is monotonic, density (pressure) and

temperature wise, whereas the decay rate of the initial stage,  $k_1$ , shows a more complex behavior with constant-density lines crossing each other above 3500 K. Moreover, their pressure variation is opposite at temperatures  $\leq 3500$  K and below 44% compression:  $k_2$  increases when pressure increases, whereas  $k_1$  decreases. Conversely, at these temperatures, raising the density from 40% compression to 44% increases the decay rate  $k_1$ . The monotonic behavior of  $k_2$  is understood as it is an averaged energy release rate representing a complex sequence of chemical reactions whose yield improves with pressure increase. On the other hand, as will be seen in the fragments analysis section, the initial decomposition reaction that influences  $k_1$  is pressure dependent, where a transition occurs between a lower pressure mechanism, C–N bond break, to a higher pressure

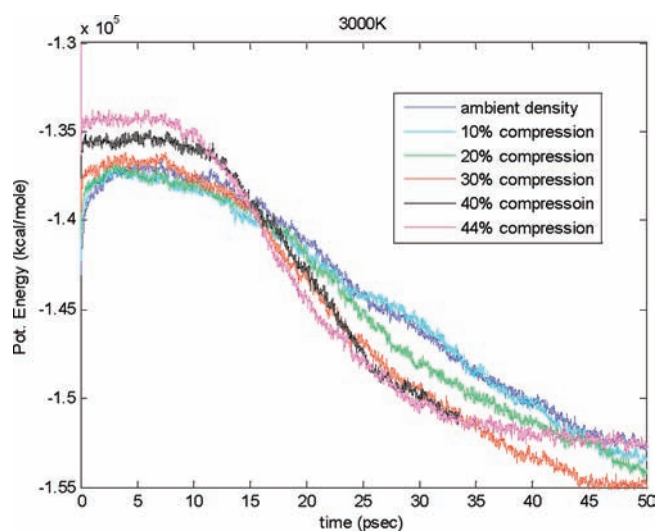


**Figure 7.** PE versus simulation time for various densities, demonstrating similar decay rates for compressions above 30%. Energy units are kcal/mol of simulation cells.

**Table 2.** Time of PE Maximum ( $t_{\max}$  [ps]) as a Function of Mass Density and Temperature

mass density [gr/cm <sup>3</sup> ]	2500 [K]	3000 [K]	3500 [K]	4000 [K]	4500 [K]
1.111	21.3	6.9	2.6	1.7	1.0
1.234	16.8	5.0	2.1	1.2	0.9
1.389	14.3	3.4	1.9	1.1	0.8
1.587	20.1	4.2	2.1	1.0	0.6
1.852	11.8	4.5	1.4	0.7	0.5
1.984	15.3	6.2	1.8	0.7	0.5

(near and above CJ pressure) route,  $\text{CH}_3\text{NO}$  production. The former is a unimolecular process, whose rate is suppressed by pressure due to collisions, and the latter fragment is formed mainly by bimolecular (or higher) reactions that speed up with pressure increase. Some of these reactions are listed in the next section.

Arrhenius parameters obtained from the exponential functions fits to NM initial decay ( $k_1$ ) and PE decay ( $k_2$ ) are listed in Tables 3 and 4 for the various densities. The Arrhenius fit for  $k_1$  was made with temperatures in the range 2500–4500 K, and in the PE fit ( $k_2$ ) temperatures  $\geq 3500$  K were used. Generally, activation energies in the initial reactions stage ( $E_{a1}$ ) are higher than those in the intermediate stage ( $E_{a2}$ ). The mean and standard deviation for  $E_{a2}$  is  $E_{a2} = 37.5 \pm 3.6$  kcal/mol.  $E_{a1}$  is almost constant for densities below 30% compression ( $49.4 \pm 1.3$  kcal/mol), and it rises with density until 44% compression where it is reduced. On the basis of the fragments analysis in the next section,  $E_{a1} = 49.4 \pm 1.3$  kcal/mol is the activation energy of C–N bond cleavage in hot liquid NM below 30% compression. This value is lower than the C–N bond dissociation energy measured in the gas phase,  $D_0 = 60.1$  kcal/mol. The difference (reduction in the activation energy by  $\sim 10$  kcal/mol) can be explained by many factors. With NM compression  $>30\%$ , the initial decomposition of NM is more complex and includes several competing reactions. These reactions are influenced by pressure change, and the activation energy reflects their mutual

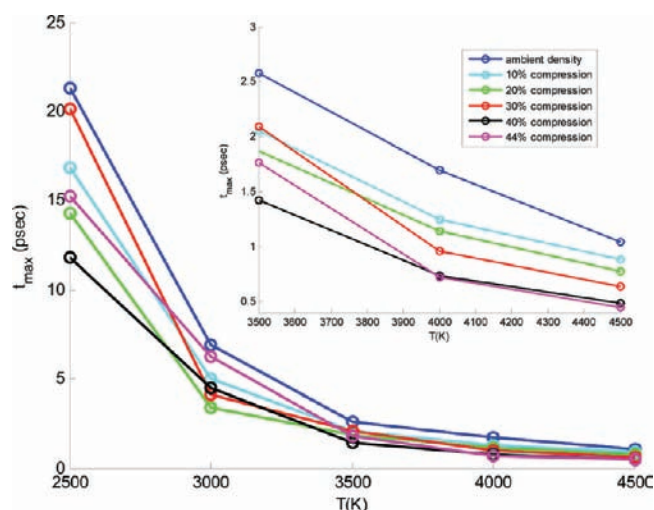


**Figure 8.** PE maximum time versus temperature for various densities. Also shown is an enlarged region between 3500 and 4500 K. At lower temperatures, PE has a flat top, and the accuracy of  $t_{\max}$  is reduced.

contribution to the initial decomposition of NM at higher densities/pressures.

In previous studies,<sup>7</sup> ReaxFF simulations of liquid NM (ambient density) in the temperature range 2200–3000 K were carried out. Effective activation energy for NM decomposition was obtained by assuming overall first-order reaction during the whole simulation period (until  $\sim 95\%$  decomposition of NM). The value of the activation energy obtained was  $\sim 33$  kcal/mol, significantly lower than  $\sim 50$  kcal/mol obtained here. In order to evaluate the difference between the two fitting approaches for  $E_a$  extraction in current simulations, a single exponential function was fitted to NM decay until the end of the simulations. The results are shown in Table 5. Comparing to Table 3 it is seen that at compressions below 30% there is a small deviation ( $<3\%$ ) between values obtained with the fitting method suggested here (time between  $[t_0, t_{\max}]$ ) and those obtained with fitting the entire simulation period. At larger compressions, the mismatch is higher (5–12%), as seen also in Figure 10. In any case, these values do not compensate for the large difference between  $E_a$  obtained here and in ref 7. These might be related to the large deviations between the fitted curves and the simulation results in ref 7, the different temperature interval, and possibly the difference in potentials used in both studies. Interestingly,  $E_{a2}$  at ambient density is 32.8 kcal/mol (see Table 4), resembling the value obtained in ref 7. It can be generally stated that when intermediate reactions evolution dominates and dictates the decay of NM molecules, the effective overall activation energy is lower.

Arrhenius parameters calibrated for liquid NM decomposition in shock initiation experiments<sup>4</sup> are  $A_0 = 2.6e9 \text{ s}^{-1}$  and  $E_a = 23$  kcal/mol. These values are lower than those obtained here (and in ref 7) for constant temperature and volume simulations.

**3.4. Fragments Analysis: Initial and Intermediate Reactions.** Fragments created in the early stages of NM decomposition are analyzed for different initial densities and temperatures using BondFrag code. Stable products, obtained at later stages of the simulation, are analyzed separately (see section 3.5). Fragments that reach over 3% of the initial amount of NM molecules

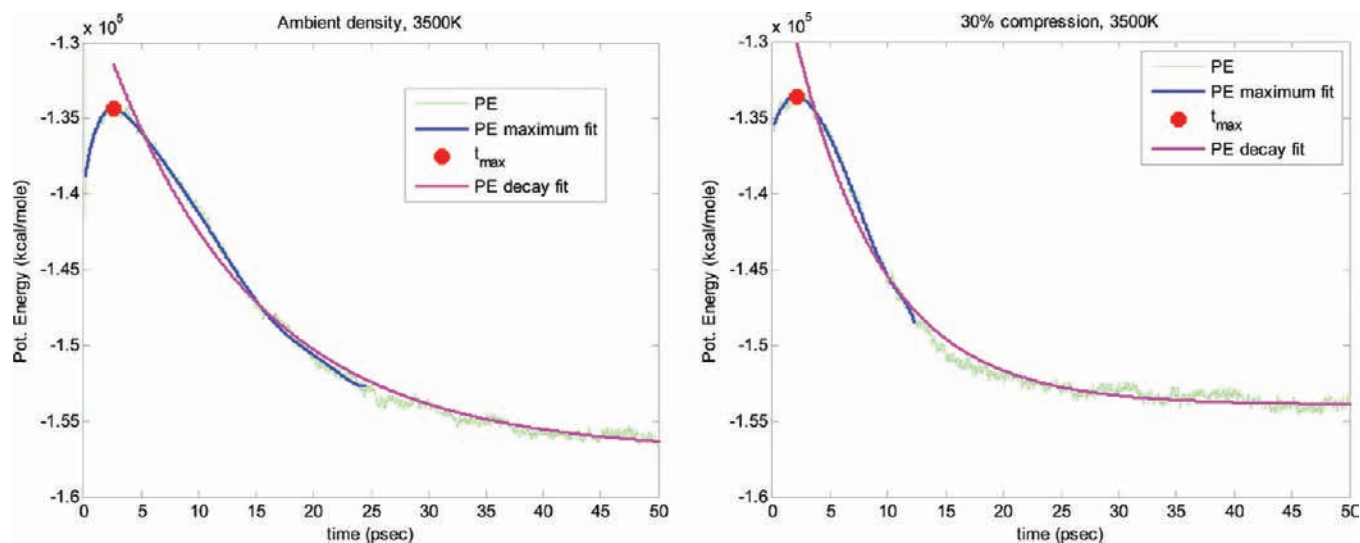


Figure 9. PE fitting for ambient density (left) and 30% compression (right) at 3500 K. Fittings for evaluation of (a) PE maximum time,  $t_{\max}$  (red point), and (b) decay rate,  $k_2$ , are shown in blue and pink, respectively.

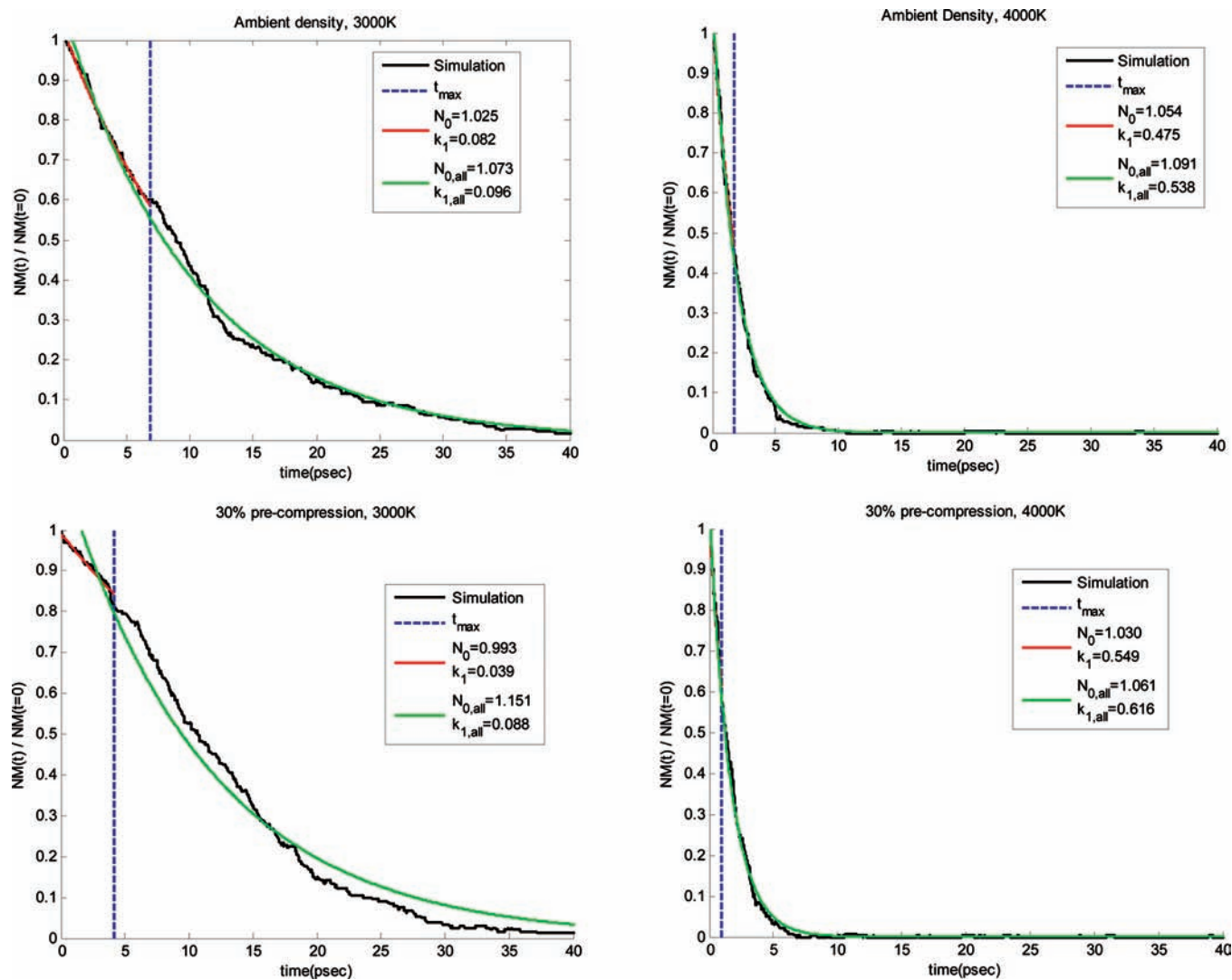
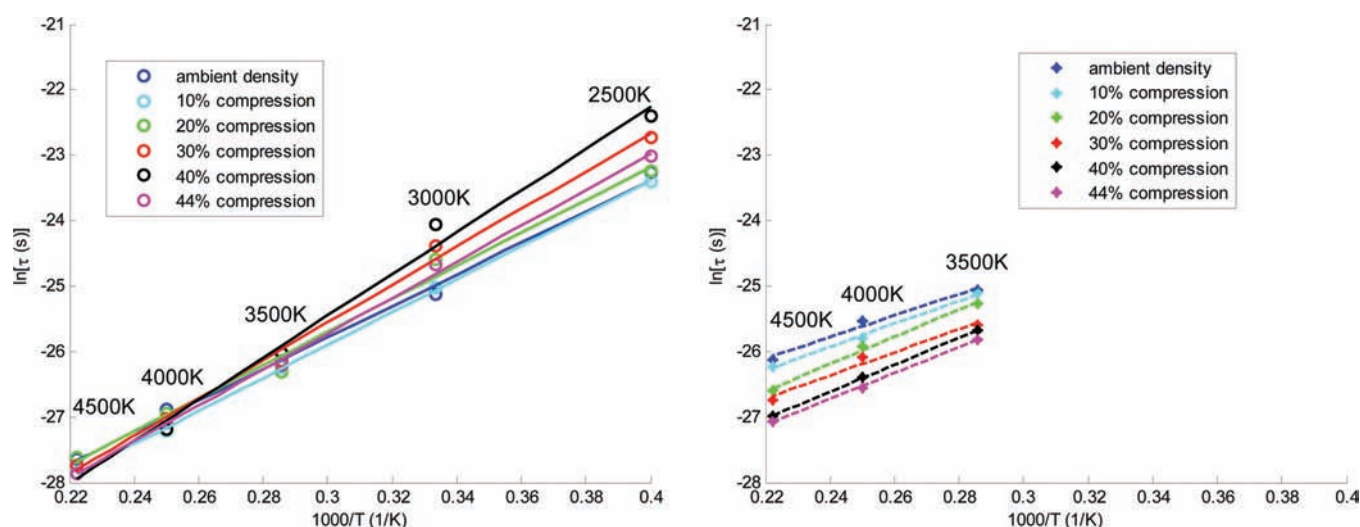


Figure 10. NM decay curve (black), for ambient density and 30% compression, in 3000 K (left) and 4000 K (right) simulations. Single exponential functions (eq 1) were fitted to each curve until  $t_{\max}$  (red) and throughout simulation length (green, denoted "all").



**Figure 11.** Arrhenius plots (shown is reaction time,  $\tau = 1/k$ ) for NM initial decomposition (left -  $k_1$ , solid lines) and PE decay (right -  $k_2$ , dashed lines), for various densities.

**Table 3.** Arrhenius Parameters Fitted to NM Exponential Decay Rates,  $k_1[\rho, T]$ , over a  $[t_0, t_{\max}]$  Time Interval for Various Initial Densities<sup>a</sup>

mass density [gr/cm <sup>3</sup> ]	$\ln(A_0[\text{s}^{-1}])$	Ea [kcal/mol]
1.111	33.0	47.9
1.234	33.5	49.9
1.389	33.3	50.3
1.587	34.2	57.4
1.852	35.0	63.4
1.984	34.0	54.6

<sup>a</sup> Temperature range used: 2500–4500 K.

**Table 4.** Arrhenius Parameters Fitted to PE Exponential Decay Rate,  $k_2[\rho, T]$ , for various initial densities<sup>a</sup>

mass density [gr/cm <sup>3</sup> ]	$\ln(A_0[\text{s}^{-1}])$	Ea [kcal/mol]
1.111	29.8	32.8
1.234	30.2	35.2
1.389	31.2	41.6
1.587	30.6	35.0
1.852	31.6	40.9
1.984	31.5	39.2

<sup>a</sup> Temperature range used: 3500–4500 K.

(240) during simulation period are presented for ambient density and various compressions (20%, 30%, 40% and 44%) at 3000 K and 4000 K in Figure 12, and at 2500 K in Figure 13.

Figure 12A (ambient density, 3000 K) shows that CH<sub>3</sub> (red line) and NO<sub>2</sub> (green line) are created rapidly at the beginning of the simulation. Around 5 ps, the rapid rise stops, and a plateau followed by decrease is seen. On the other hand, the CH<sub>3</sub>NO fragment (blue dashed line) is not created initially; only after ~2 ps does its amount rise at a relatively slow rate.

Figure 12B (20% compression, 3000 K) again shows a rapid growth of CH<sub>3</sub> and NO<sub>2</sub> fragments as simulation begins. After ~3 ps, the CH<sub>3</sub>NO amount starts to increase at a high rate (relative to the growth in Figure 12A), while CH<sub>3</sub> and NO<sub>2</sub> production stops. At ~5 ps, the concentration of CH<sub>3</sub>NO surpasses that of CH<sub>3</sub>. On the basis of this behavior, it is concluded that CH<sub>3</sub> and CH<sub>3</sub>NO are produced by competitive reactions, and the creation of one inhibits the formation of the other.

Figure 12C (30% compression, 3000 K) shows that already at the beginning of the simulation both NO<sub>2</sub> and CH<sub>3</sub>NO are produced at the same rate. CH<sub>3</sub>NO becomes the most abundant fragment within the simulation time shown. Note that CH<sub>3</sub> concentration is very low (<3%) compared to its maximal amount with 20% compression (~8%) and at ambient density (~15%). This is due to its quick consumption by other reactions at high densities (e.g., with NM molecule or H atom).

**Table 5.** Arrhenius Parameters Fitted to NM Exponential Decay Rates,  $k_1[\rho, T]$ , over the Entire Simulation Period for Various Initial Densities<sup>a</sup>

Mass density [gr/cm <sup>3</sup> ]	$\ln(A_0[\text{sec}^{-1}])$	Ea [kcal/mol]
1.111	33.0	46.8
1.234	33.3	48.4
1.389	33.8	51.8
1.587	33.9	52.3
1.852	34.5	56.2
1.984	34.7	57.4

<sup>a</sup> Temperature range: 2500–4500 K.

In Figure 12D,E (40% and 44% compression, 3000 K) CH<sub>3</sub>NO is by far the dominant fragment in the initial and intermediate stages of NM decomposition.

A more detailed investigation of the difference in the *initial* decomposition mechanism of liquid NM as a function of density is demonstrated in Figure 14. Here, the number of broken C–N bonds as a function of time is calculated at 3000 K for all densities studied (left). It is clearly seen that C–N bond scission is inhibited by the density increase. Initially ( $t < 1$  ps), at all densities, there is some amount of C–N bonds breaking. However, below 30% compression, the quantity of broken

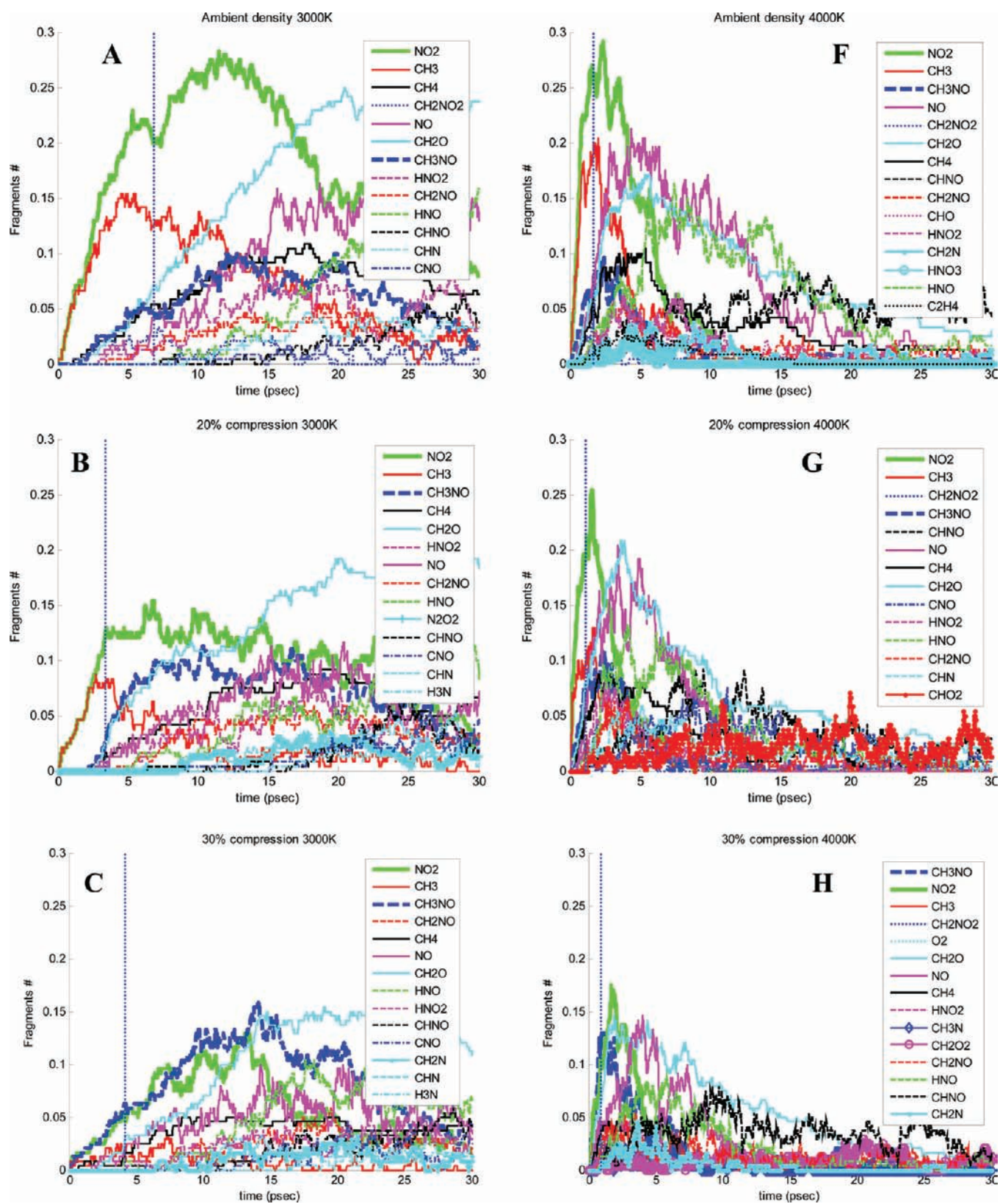
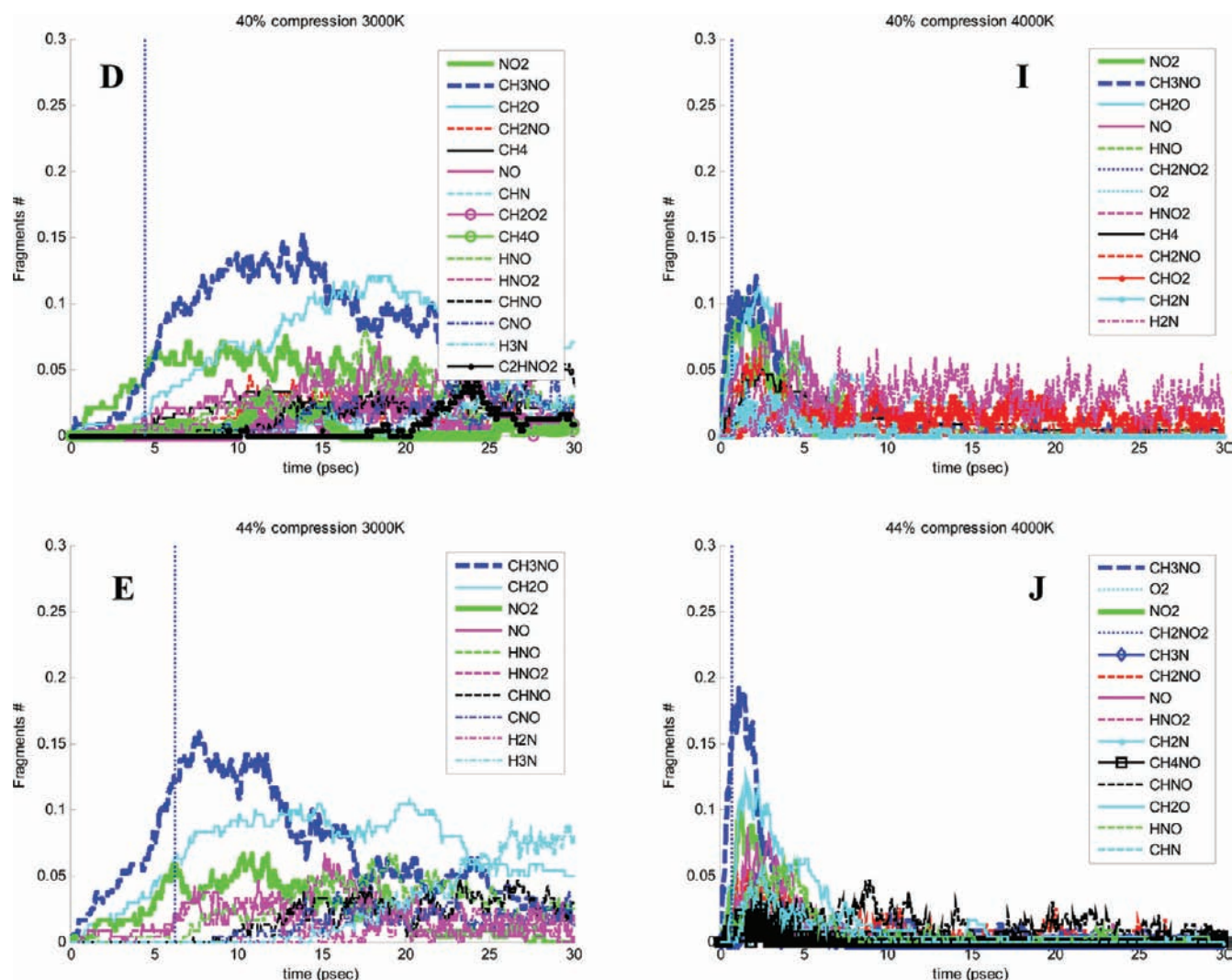


Figure 12. Continued



**Figure 12.** Initial and intermediate fragments obtained in 3000 K and 4000 K simulations at various densities. Dashed vertical lines are  $t_{\max}$  (PE maximum). Shown are fragments reaching  $>3\%$  of initial NM molecules, normalized relative to 240 initial NM molecules.

C–N bonds keeps increasing at a pronounced faster rate compared to the growth of broken C–N bonds at higher densities. On the right-hand side of Figure 14, the total number of broken C–N bonds per density is shown at 7 psec. There is a sharp transition from the high amount of total broken C–N bonds at lower densities ( $>35\%$ ) to the smaller amount at compressions above 30% ( $<25\%$ ).

In summary, the analysis of the initial decomposition reactions and fragments of hot liquid NM shows that they are density dependent:

1. Below 30% compression, the first reaction is a unimolecular C–N bond break forming  $\text{CH}_3$  and  $\text{NO}_2$ . Then, after some time delay ( $\sim t_{\max}$ ), a variety of intermediate reactions occur producing mostly  $\text{CH}_3\text{NO}$ ,  $\text{CH}_2\text{O}$ ,  $\text{CH}_4$ ,  $\text{NO}$ , and  $\text{HNO}_2$ .
2. At 30% compression, the amount of the two competing initial fragments,  $\text{NO}_2$  and  $\text{CH}_3\text{NO}$ , is about equal. After some delay, the third abundant fragment,  $\text{CH}_2\text{O}$ , is created together with others. At yet higher compressions, the dominant initial fragment becomes  $\text{CH}_3\text{NO}$ , and C–N

bond breaking is inhibited. Additional fragments formed at smaller amounts in the intermediate decomposition stage at high compressions are  $\text{CH}_2\text{O}$ ,  $\text{NO}_2$ ,  $\text{NO}$ ,  $\text{CH}_4$ , and  $\text{HNO}_2$ .

The density of NM at 30% compression,  $1.587\text{gr}/\text{cm}^3$ , is close to CJ density,  $1.596 \pm 0.02\text{ gr}/\text{cm}^3$ , and the temperatures employed in the simulations are in the vicinity of CJ temperature ( $\sim 3000\text{ K}$ ). It is interesting to compare the initial pressure obtained in the NVT simulations studied, where decomposition of NM begins, with CJ pressure. In Table 6, approximate values of the initial pressures are given for various NVT simulations. As can be seen, only above 30% compression the pressure is higher than CJ pressure,  $13 \pm 0.4\text{ GPa}$ . Under these conditions the initial fragment formed is  $\text{CH}_3\text{NO}$ . Hence, it can be concluded that above 30% compression the leading fragment formed in the initial step of liquid NM detonation is  $\text{CH}_3\text{NO}$ .

The general density-dependent trend described above is not temperature dependent (see 4000 K and 2500 K results in Figure 12F–J and Figure 13A–E, respectively). The main effect of temperature is speeding up the reactions.

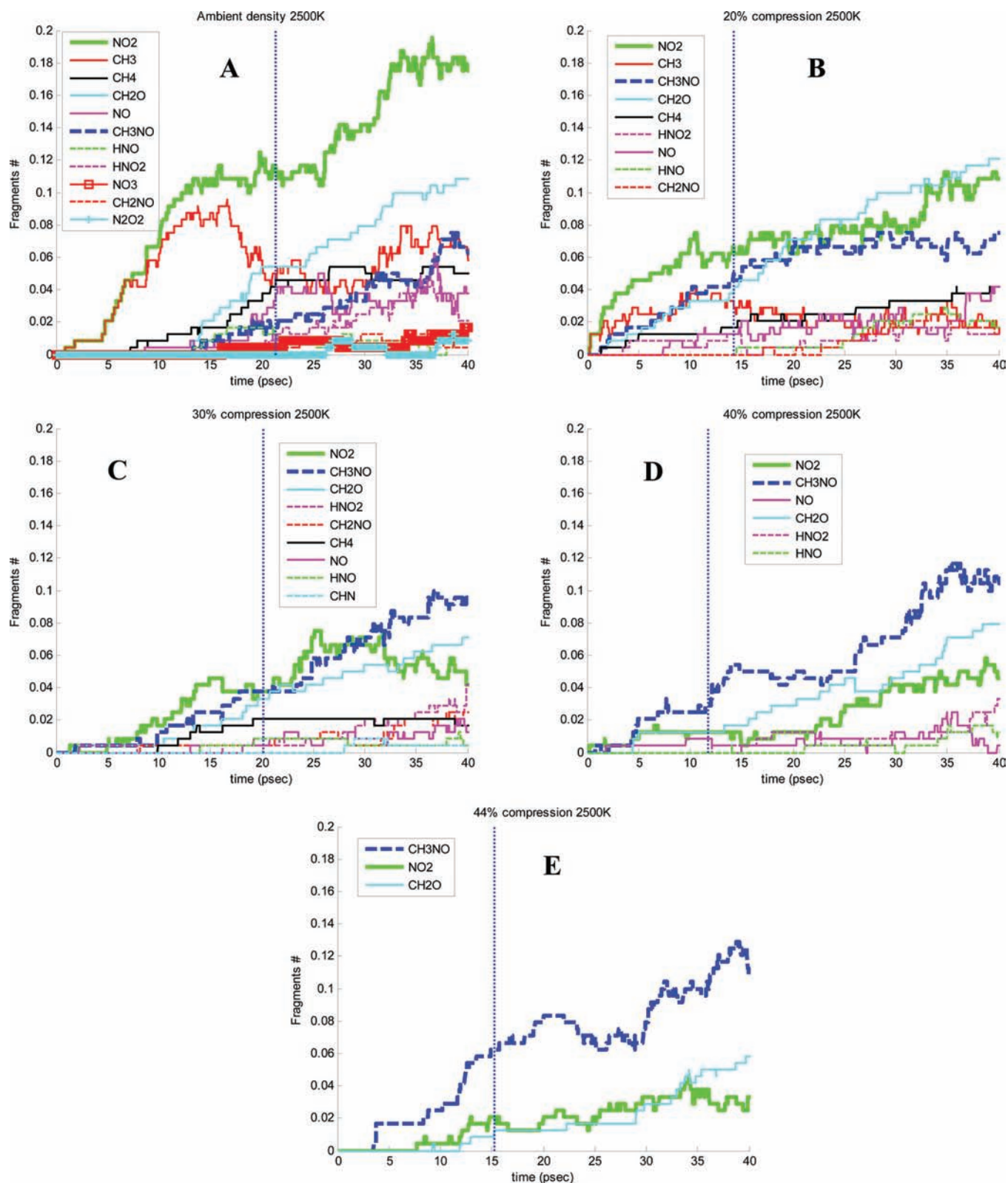


**Figure 13.** Initial and intermediate fragments in 2500 K simulations at various densities. See caption in Figure 12.

In Figures 12 and 13, the time where PE reaches its maximal value,  $t_{\text{max}}$  is marked (vertical blue dashed line). As can be seen, it is closely related to the onset of secondary reactions where a variety of exothermic reactions occur.

In Figure 15, the time evolution of NO<sub>2</sub> (left) and CH<sub>3</sub>NO (right) fragments is shown as a function of initial density at 3000 K and 4000 K. As can be seen, NO<sub>2</sub> fragment amount and production rate monotonically decrease as

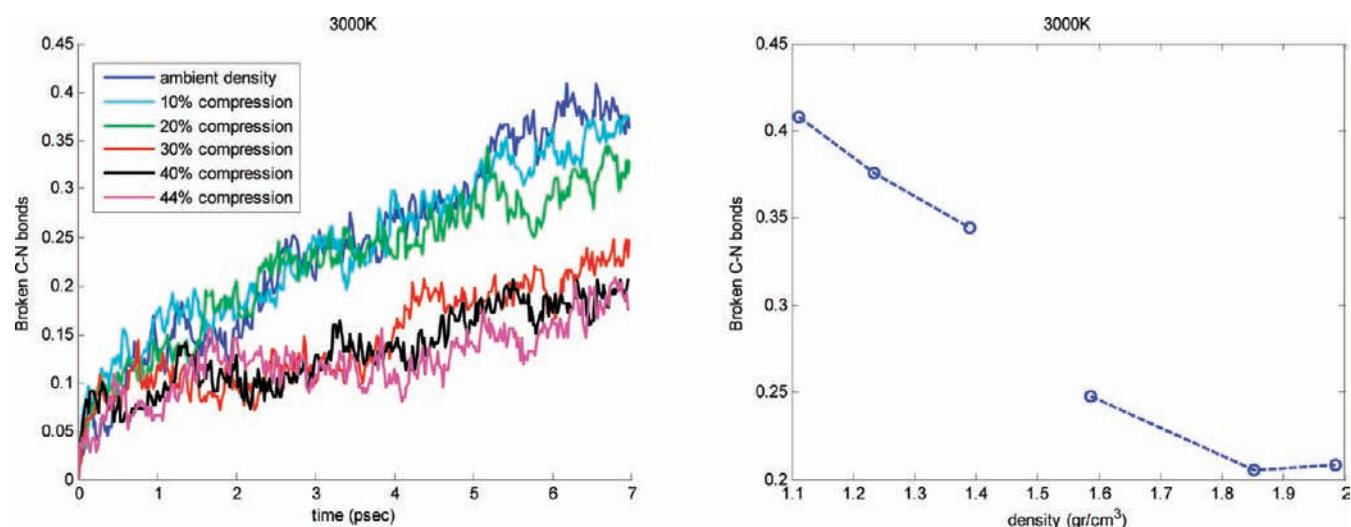


**Figure 14.** Left: Time dependence of broken C–N bonds as a function of density. Right: Total number of broken C–N bonds at 7 ps, as a function of density. The broken bonds number is normalized by the initial NM molecules (240).

density/pressure increases. On the other hand,  $\text{CH}_3\text{NO}$  overall amount increases with density. As seen above, at lower densities there is almost no production of  $\text{CH}_3\text{NO}$  at the beginning of NM decomposition, whereas at higher densities ( $\geq 30\%$  compression) it is created as soon as the decomposition begins.

Figure 15 demonstrates the correlation between the competing reactions governing the initial production of these fragments: At low densities C–N unimolecular bond break is energetically favorable (lower activation barrier,  $\sim 50$  kcal/mol; see Table 3). At higher densities, the unimolecular reaction is suppressed, via collisions with surrounding molecules that absorb energy from the excited molecule. At the same time, with these higher densities, bimolecular reactions that produce  $\text{CH}_3\text{NO}$  become dominant due to more frequent and effective collisions, whereas they are inferior energetically at lower compressions (e.g., N–O bond scission in the gas phase of NM is highly endothermic,<sup>24</sup>  $D_0 = 94.7$  kcal/mol).

Here also, increasing the temperature accelerates the reactions but does not quantitatively modify the density tendency described above.

Under the high densities and temperatures studied here, the assignment of atoms to molecules is not unique. However, on average, the trends of fragments creation are trustworthy. Some of the leading reactions in the initial and intermediate decomposition stages of NM obtained from BondFrag analysis are (main fragments are bold-faced):

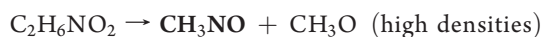
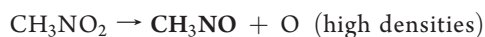
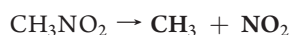
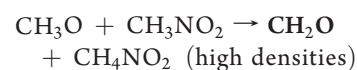
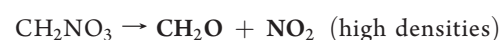
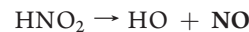
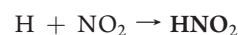


**Table 6.** Approximate Minimal Pressures (GPa) Reached in the Initial Stage of NM Decomposition with Various Densities and Temperatures<sup>a</sup>

density [gr/cm <sup>3</sup> ]	2500 K	3000 K	4000 K
1.111	<3	3.2	4.5
1.389	5.3	6	8.5
1.587	8.4	10	12
1.852	15	16.5	20
1.984	20	21.5	25

<sup>a</sup> Values were taken from Figure 6.



Unless specified, the above reactions occur at all compressions. Excluding the first reaction, the fragments react among themselves or decompose to smaller species.

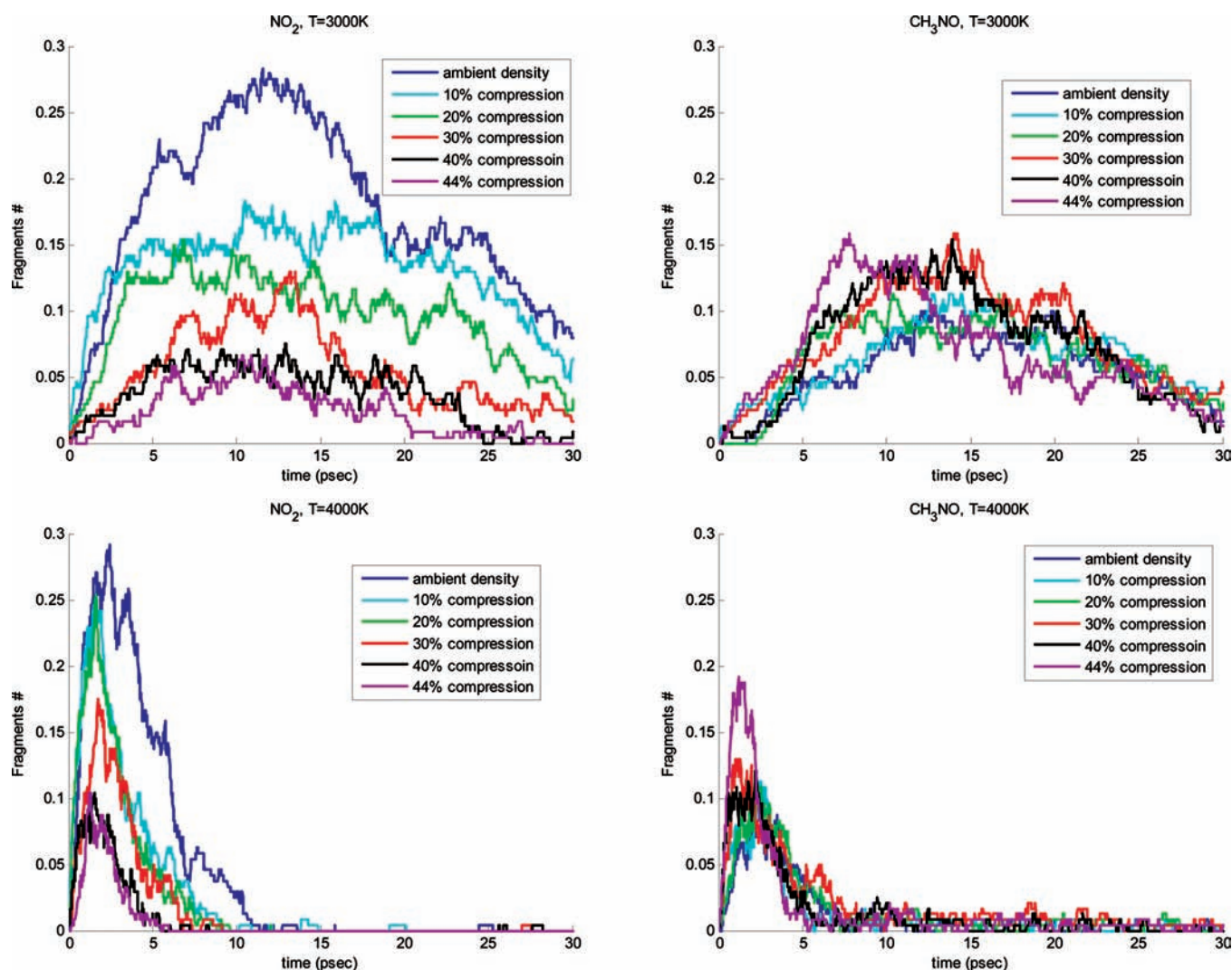


Figure 15.  $\text{NO}_2$  (left) and  $\text{CH}_3\text{NO}$  (right) fragments time evolution as a function of density at 3000 K and 4000 K.

Some additional reactions that produce fragments participating in these reactions are



As can be seen, some of the above are autocatalytic reactions, involving parent NM molecules.

**3.5. Final Products Analysis: Formation and Asymptotic Amounts.** The main products obtained in the thermal decomposition of NM are  $\text{N}_2$ ,  $\text{H}_2$ ,  $\text{H}_2\text{O}$ ,  $\text{CO}_2$ ,  $\text{CO}$ ,  $\text{NH}_3$ , and  $\text{OH}$ . Note that *no* significant amount of stable, carbon-rich clusters was observed among the fragments produced in the present simulations. This implies that NM detonation is not expected to

produce carbon soot or carbon clusters, unlike TATB<sup>20</sup> or trinitrotoluene (TNT).<sup>26</sup>

An increasing exponential function (see eq 4) was fitted to the time evolution curves of these products in simulations where the final products approached saturation values. In Figure 16, simulation results and fitted curves are presented for various densities at 4000 K, and asymptotic amounts extracted per product are listed in Table 7. The latter are plotted in Figure 17 as well as measured liquid NM detonation products.<sup>22</sup> Both in measurement and calculations, the most abundant product is  $\text{H}_2\text{O}$ . As seen, excluding  $\text{NH}_3$ ,  $\text{OH}$  and  $\text{H}_2\text{O}$ , the amount of all calculated fragments is reduced when pressure increases. There is a very good agreement between the experimental and calculated amounts of all measured products, excluding  $\text{CO}$ . It should be noted that the experimental values were measured after expansion and cooling down of the gaseous products, whereas the calculated products are at the same density and temperature as the original liquid NM. The  $\text{OH}$  fragment is unstable at ambient conditions, but is obtained in our simulations. Assuming  $\text{OH}$  combines with  $1/2 \text{H}_2$  molecule to produce  $\text{H}_2\text{O}$  during cooling and decompression, the amount of  $\text{H}_2\text{O}$  expected to be obtained when ambient conditions are reached is also plotted in Figure 17

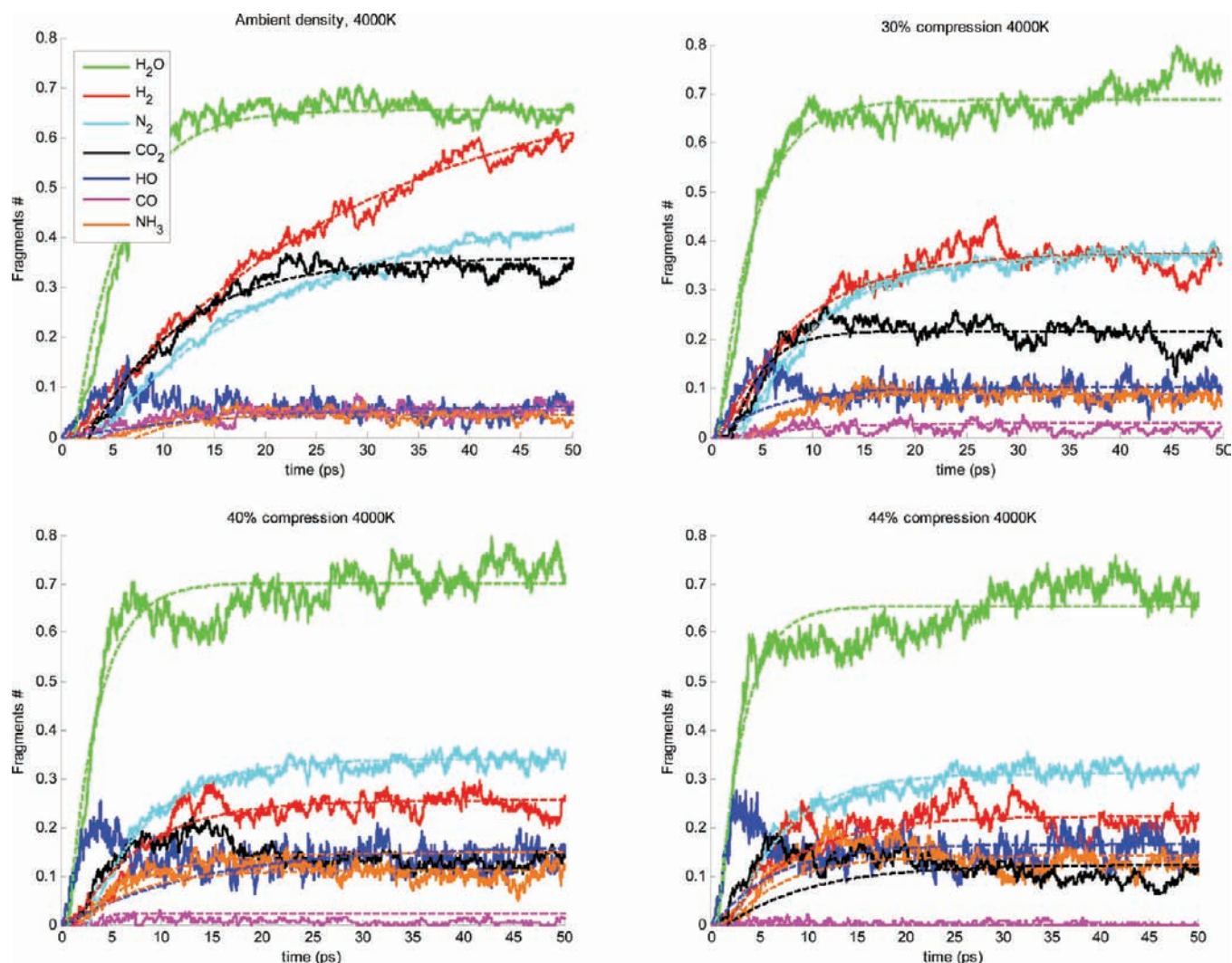


Figure 16. Products creation (solid lines) and increasing exponential functions fits (dashed lines, see eq 4) at 4000 K and various compressions.

Table 7. Final Products Asymptotic Amounts at 4000 K and Various Densities<sup>a</sup> ( $d_0$  represents the Calculated Density at Ambient Conditions)

fragment	$d_0$	$1.1d_0$	$1.2d_0$	$1.3d_0$	$1.4d_0$	$1.44d_0$
OH	0.066	0.080	0.088	0.102	0.161	0.165
H <sub>2</sub>	0.730	0.572	0.542	0.375	0.255	0.223
H <sub>2</sub> O	0.655	0.663	0.654	0.687	0.703	0.654
CO	0.054	0.047	0.035	0.029	0.022	<0.02
N <sub>2</sub>	0.447	0.406	0.412	0.374	0.340	0.311
CO <sub>2</sub>	0.360	0.314	0.288	0.217	0.148	0.123
NH <sub>3</sub>	0.046	0.052	0.075	0.088	0.111	0.141

<sup>a</sup>Values are normalized with respect to the initial amount of NM molecules.

(dotted green line). The agreement between the calculated H<sub>2</sub>O amount at CJ density and the measured value improves, and the deviation between the measured and calculated amounts of H<sub>2</sub> decreases (not shown).

Finally, in Figure 18, gaseous product isotherms are plotted at various temperatures. Note that the product composition varies with

temperature and density. The isotherms were produced from *final* total pressure values per simulation (Figure 6). At 3000 K, the product formation may possibly not be fully completed within the simulation time, thus the accuracy of this products isotherm is slightly lower.

**3.6. Decomposition Reactions Exothermicity and Change of Enthalpy.** Two additional parameters that can be obtained from the MD simulations are decomposition exothermicity,  $\Delta U_{\text{exo}}$  (eq 2), and enthalpy change (eq 3). These quantities are a measure of the exothermic part in the NM decomposition process. In Figure 19,  $\Delta H$  is plotted as a function of density for the temperatures 3500, 4000, and 4500 K. As seen, the exothermicity temperature dependence is relatively weak (<10%). However, a pronounced modification in  $\Delta H$  occurs when density varies, as can be seen in Figure 19: As density increases,  $\Delta H$  increases (less exothermic), until ~30% compression where the slope is reversed and  $\Delta H$  decreases with density (more exothermic). This change might be related to the transition from initial decomposition of NM by the C–N bond break (low densities) to initial CH<sub>3</sub>NO fragment formation (higher compressions). Apparently, in the low compression range (<30%), as C–N bond cleavage is reduced with density rise, the decomposition process is less exothermic, while in the higher compression

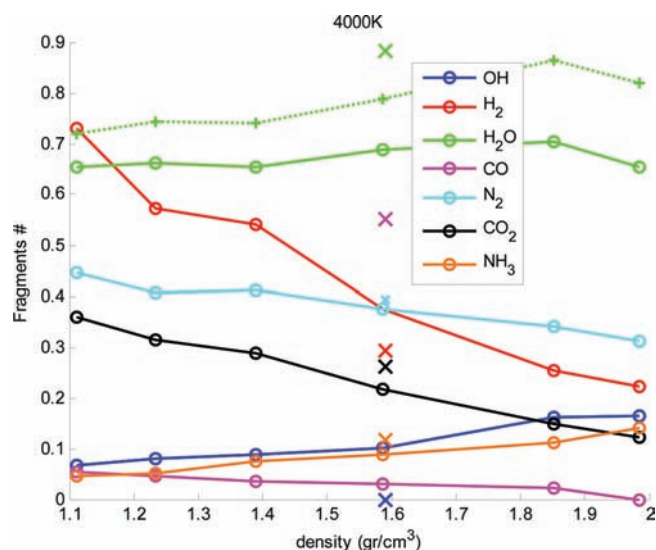


**Figure 17.** Calculated stable fragments fraction as a function of NM density at 4000 K (○, solid lines). Crosses represent measured detonation products<sup>22</sup> (plotted at CJ density). Also shown is the sum of H<sub>2</sub>O and OH fragments (+, dotted line).

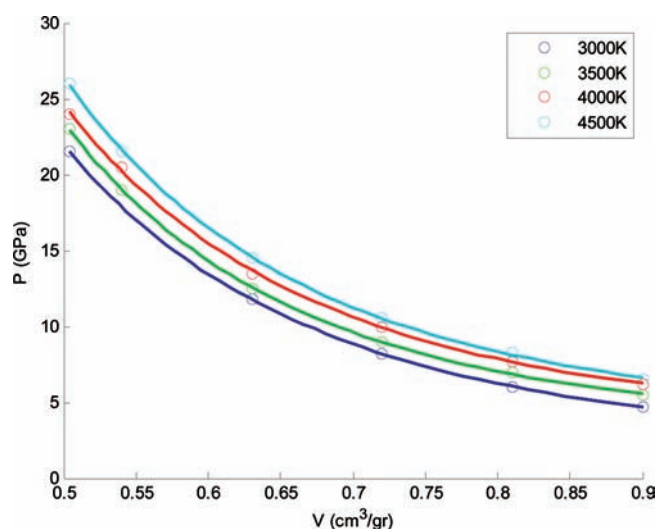


**Figure 18.** Liquid NM final product isotherms. The circles are calculation results, and the lines are second-order polynomial fits to them.

regime, the NM decomposition becomes more exothermic, in accordance with CH<sub>3</sub>NO fragment enhanced production.

In Figure 20, the contributions to enthalpy change are presented ( $\Delta U_{\text{exo}}$  and  $V\Delta P$ ). As seen, the density variation of  $\Delta U_{\text{exo}}$  is slow and monotonic, but  $V\Delta P$  shows a more pronounced change.

The measured heat of reaction for liquid NM detonation in calorimetric bomb experiments<sup>22</sup> is  $1227 \pm 7$  cal/g, which is in very good agreement with the  $\Delta H$  calculated at ambient density (see Figure 19): <3% deviation, depending on temperature. Note that Tarver uses 1060 cal/g as the NM heat of reaction for his detonation model.<sup>25</sup>

**3.7. Diffusion Coefficients Analysis.** MSDs for the four atomic constituents of NM (C, H, N, O) were calculated for ambient and 30% compression at 3000 K and 4000 K, as presented in Figures 21

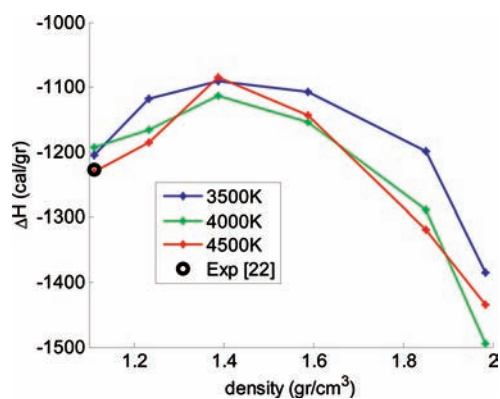


**Figure 19.** NM decomposition enthalpy change versus density for various temperatures. Also marked is the measured heat release in NM detonation<sup>22</sup> (plotted at ambient density).

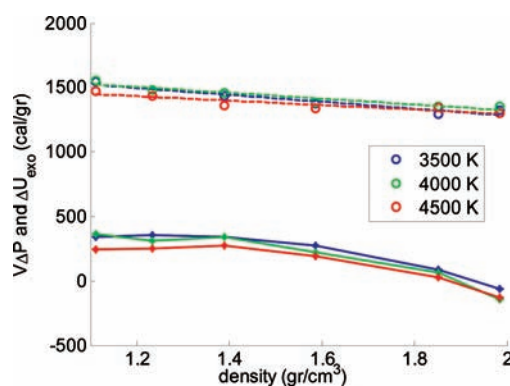


**Figure 20.** The density dependence of the energy contributions to enthalpy change: PE change (dashed lines) and  $V\Delta P$  (solid lines) for various temperatures.

and 22. The atomic coordinates used in the calculation were corrected to remove periodic boundary conditions. As expected, the atoms mobility increases with temperature and decreases when pressure (density) rises. The density dependence of the calculated MSD for hydrogen and carbon atoms is presented in Figure 23 at 3000 K.

The diffusion coefficient can be determined using eq 5 as the slope of MSD time variation. As can be seen in Figure 21 and Figure 22, in the beginning of NM decomposition (initial and intermediate reactions stages) the mobility of all atoms is similar, whereas after a time interval,  $t_b$ , the slopes break and the atomic MSD lines split ( $t_b \sim 15$  ps and  $\sim 5$  ps at 3000 and 4000 K, respectively). The slope increase for hydrogen atoms is most pronounced, whereas for carbon atoms the diffusion coefficient remains almost constant throughout the simulation. The behavior of nitrogen and oxygen atoms resembles that of hydrogen, but with smaller slope differences. The slope change time is longer than  $t_{\text{max}}$  and seems to be related to decomposition reaction stage where final products approach saturation values.

In Tables 8 and 9, diffusion coefficients obtained by fitting the MSD curve in two time regions,  $[t_0 t_b]$  ( $D_1$ ) and  $[t_b t_{\text{end}}]$  ( $D_2$ , where  $t_{\text{end}}$  is the simulation length) are summarized for 3000 and 4000 K, respectively, at various densities.

Finally, comparison between  $D_1$  and  $D_2$  values as a function of density is plotted in Figure 24 for 3000 and 4000 K and all atoms. Generally, diffusion coefficients in the later stage of decomposition

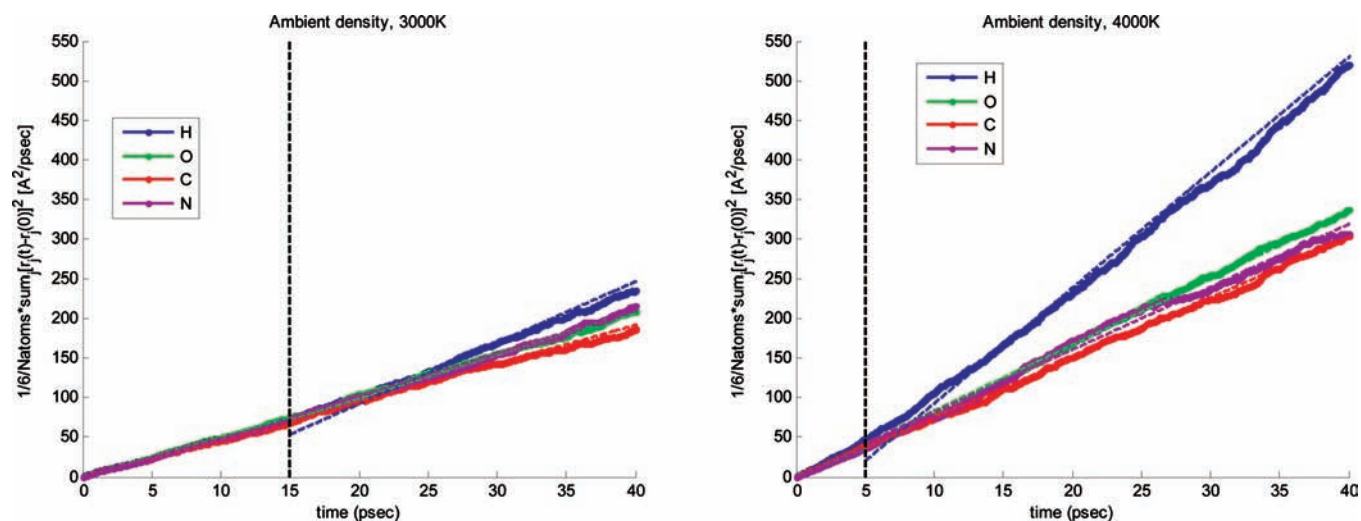


Figure 21. MSD of NM atoms during simulations at ambient density at  $T = 3000$  K and  $4000$  K. Vertical line marks  $t_b$ . Linear fits to the time intervals  $[0, t_b]$  and  $[t_b, t_{\text{end}}]$  are also shown as thin dashed lines.

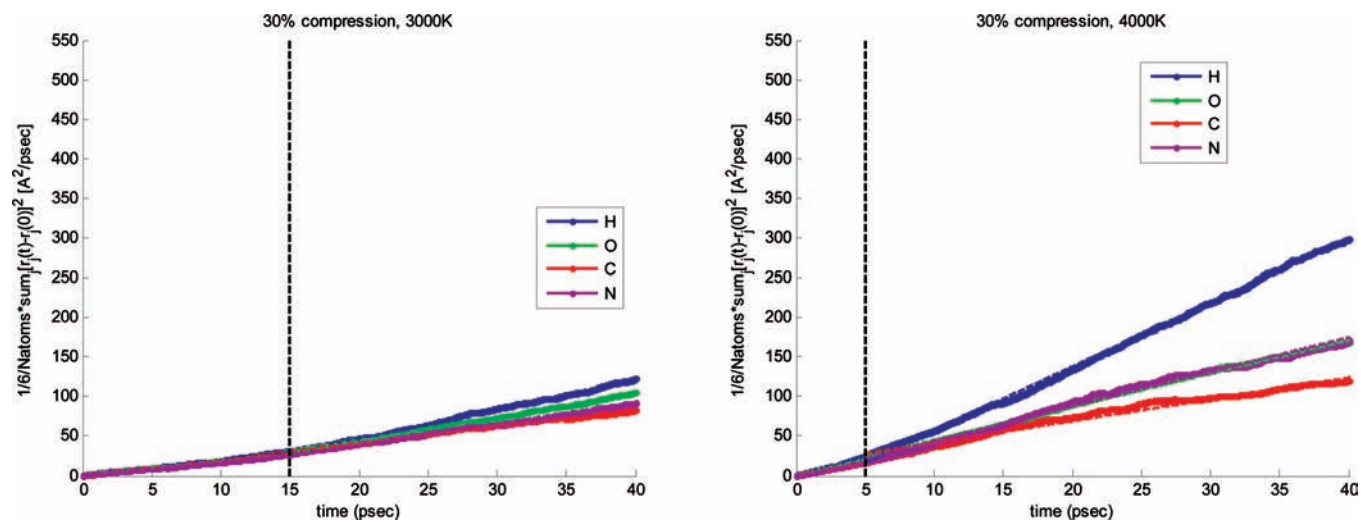


Figure 22. Same as Figure 21, for 30% compression.

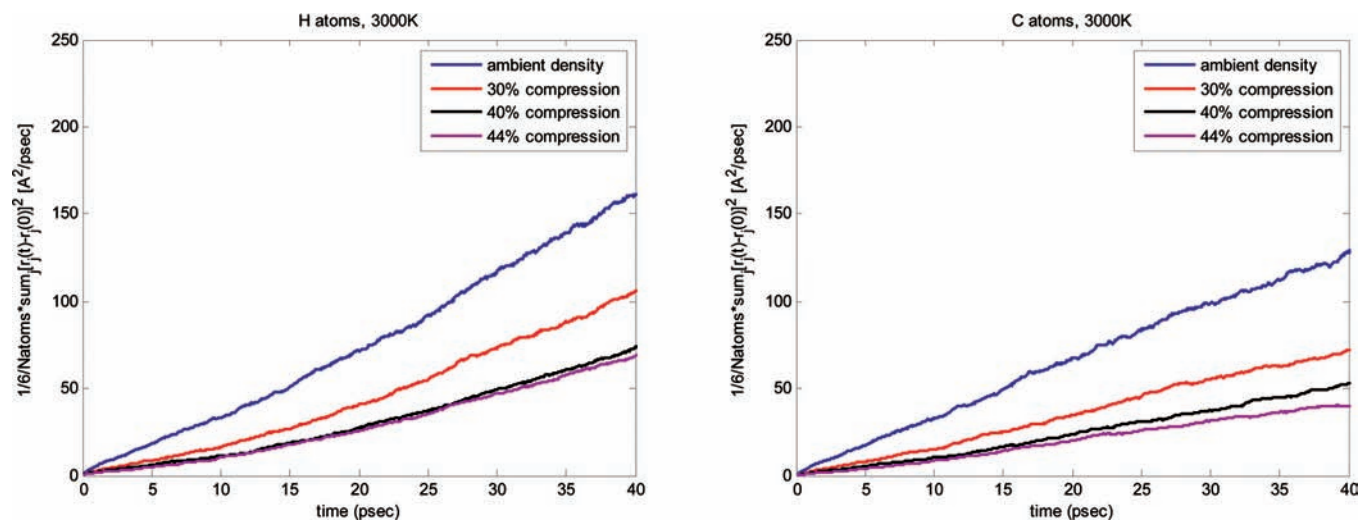


Figure 23. MSD for H (left), and C (right) atoms at various densities and  $T = 3000$  K.

reactions ( $D_2$ ) are larger than those in the initial stage ( $D_1$ ). This is due to the progress of exothermic reactions, transferring PE to kinetic energy of the formed fragments. The difference between  $D_1$

**Table 8. Atomic Diffusion Coefficients in the Time Region  $[t_0, t_b]$  of NM Decomposition ( $D_1$ ) ( $T = 3000/4000$  K)**

density [g/cm <sup>3</sup> ]	$D_H$ [Å <sup>2</sup> /ps]	$D_O$ [Å <sup>2</sup> /ps]	$D_C$ [Å <sup>2</sup> /ps]	$D_N$ [Å <sup>2</sup> /ps]
1.111	4.6/9.2	4.9/7.0	4.4/7.8	4.8/7.2
1.587	2.0/4.7	1.9/3.9	1.9/3.2	1.7/3.5
1.852	1.1/3.5	1.1/2.7	1.0/2.1	1.0/2.3
1.984	1.1/3.4	1.0/2.5	0.9/1.9	1.0/1.9

**Table 9. Atomic Diffusion Coefficients in the Time Region  $[t_b, t_{end}]$  of NM Decomposition ( $D_2$ ) ( $T = 3000/4000$  K)**

density [g/cm <sup>3</sup> ]	$D_H$ [Å <sup>2</sup> /ps]	$D_O$ [Å <sup>2</sup> /ps]	$D_C$ [Å <sup>2</sup> /ps]	$D_N$ [Å <sup>2</sup> /ps]
1.111	7.7/14.6	5.5/8.3	4.9/7.6	5.4/7.9
1.587	3.7/8.1	3.0/4.2	2.1/2.7	2.7/4.4
1.852	2.5/5.2	1.8/2.9	1.4/1.8	1.9/3.3
1.984	2.2/4.9	1.6/2.6	1.1/1.5	1.4/2.8

and  $D_2$  is maximal for hydrogen atoms and minimal for carbon atoms. In addition, as mentioned above, both diffusion coefficients decrease when pressure increases.

In Figure 25 the averaged time derivative of the atomic MSD, denoted hereafter as averaged local diffusion coefficient (ALDC), is shown for all atoms in 3000 K heat-up simulations with ambient density and 44% compression. [A filter is used to smooth out short-term fluctuations and highlight longer-term trends of the time derivative of the atomic MSD. A forward and reversed direction equal weight filter was applied, with 300 points (6 ps) window in each direction.] The ALDC curves are more sensitive to the reaction dynamics than the monotonous MSD curves, and can be used to differentiate between time periods where chemical reactions occur and diffusion-dominated non-reactive ones. In nonreactive time periods, the ALDC curve is expected to be constant. The atomic ALDC includes contributions from all relevant fragments at a given time.

Figure 26 illustrates the correlation between the hydrogen atoms ALDC curves and the time evolution of fragments that include hydrogen atoms. When such fragments are created at a high rate, the calculated hydrogen ALDC increases, and when the fragment creation rate slows down, the ALDC curve slope

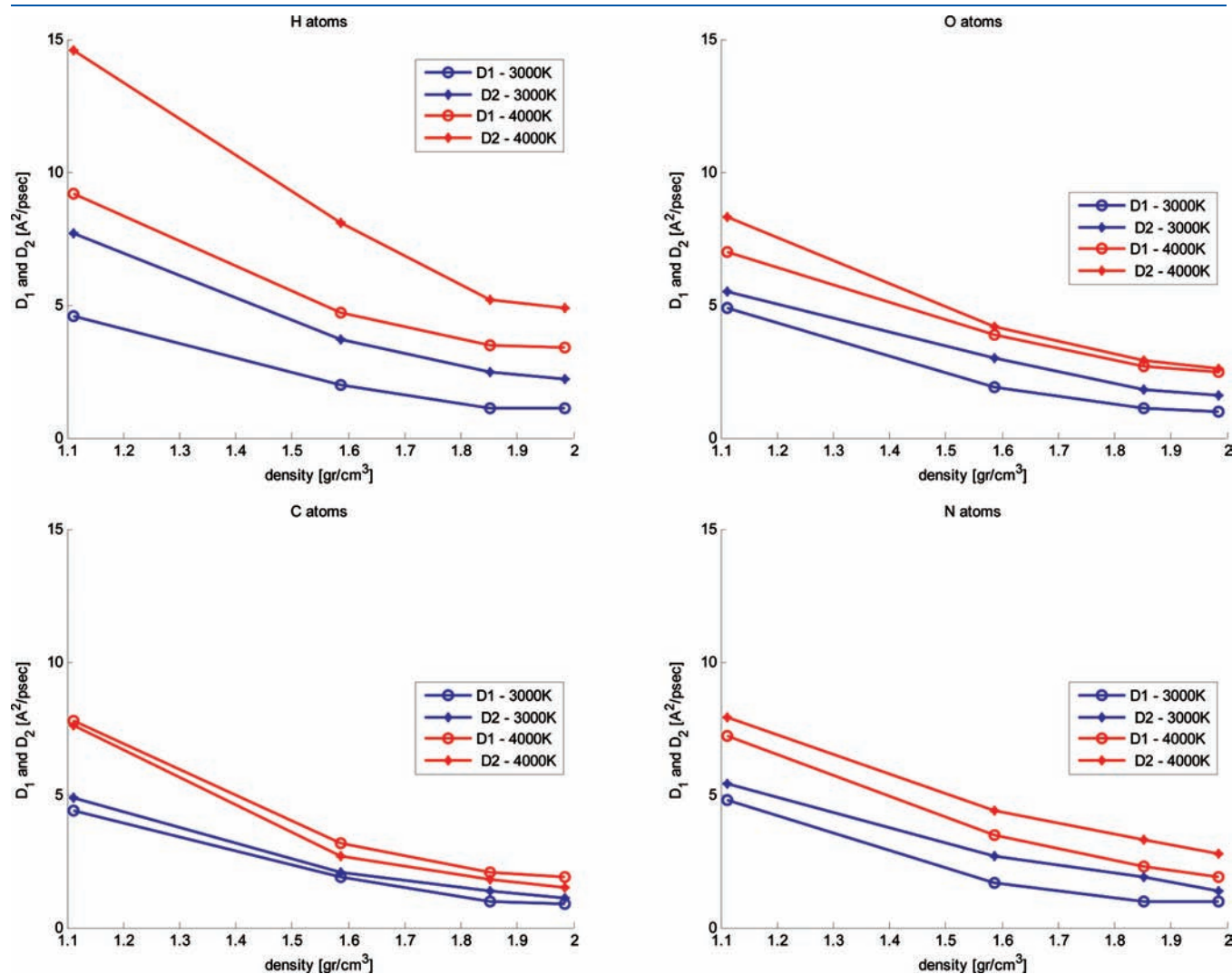


**Figure 24.** Diffusion coefficients in the time region  $[t_0, t_b]$  ( $D_1$ ) and  $[t_b, t_{end}]$  ( $D_2$ ), as a function of density, for hydrogen, oxygen, carbon, and nitrogen atoms.

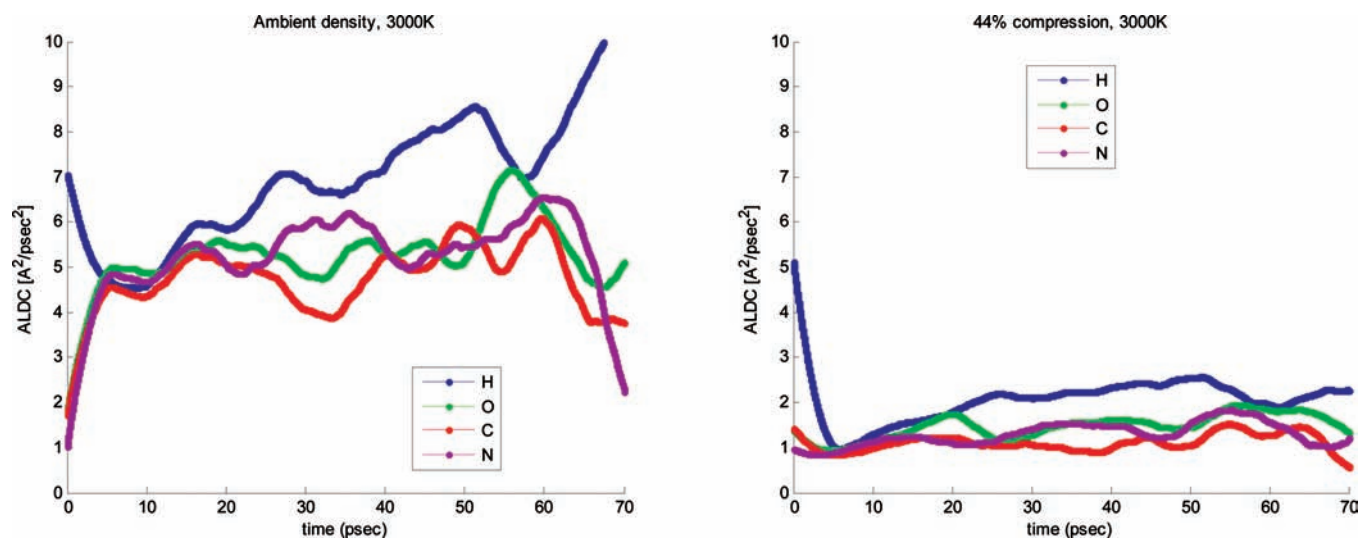


**Figure 25.** Atomic ALDC curves for ambient density (left) and 44% compression (right) simulations at 3000 K (note that the initial values of the curves have no physical significance at times shorter than the filter time-window, 6 ps).

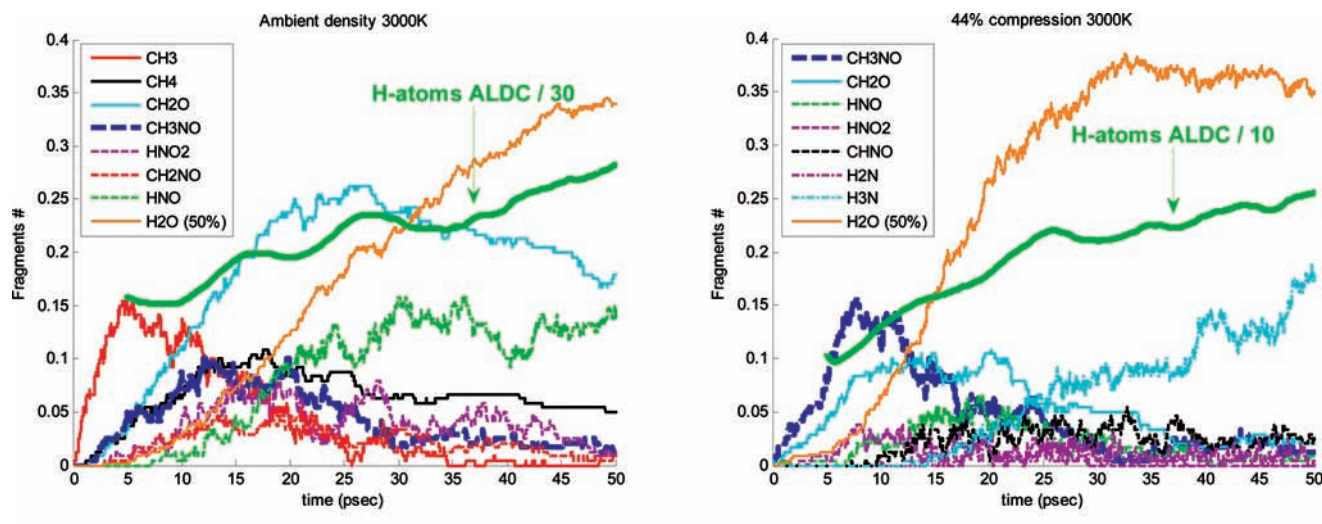


**Figure 26.** Evolution of the primary hydrogen containing fragments formed in 3000 K simulations at ambient density (left) and 44% compression (right), versus hydrogen ALDC (thick green line). For clarity, ALDC is divided by 30 (10) for the ambient density (44% compression) simulation, and the amount of H<sub>2</sub>O molecules is halved.

becomes more moderate and can become negative. This dynamic correlation is more pronounced for hydrogen atoms and is weaker for heavier atoms.

## CONCLUSIONS

The decomposition kinetics of hot liquid NM was studied at densities varying from ambient density to 44% compression, and at temperatures in the range 2500–4500 K using ReaxFF MD simulations. A change of mechanism was observed in the initial stage of NM decomposition as a function of density:

- At lower densities, the unimolecular C–N bond cleavage is the dominant reaction, producing CH<sub>3</sub> and NO<sub>2</sub> fragments.
- As density and pressure rise approaching CJ detonation conditions (~30% compression, ~3000 K) the dominant mechanism switches to the formation of the CH<sub>3</sub>NO fragment via H-transfer and/or N–O bond rupture.

This behavior leads to a different kinetic and energetic behavior, as well as products distribution, depending on the density.

Thermal rate constants were calculated for the initial ( $k_1$ ) and intermediate ( $k_2$ ) decomposition stages of NM. Their density dependence is opposite at temperatures  $\leq 3500$  K and below 44% compression:  $k_2$  increases when density increases, whereas  $k_1$  decreases. At these temperatures, however,  $k_1$  increases when the compression increases from 40% to 44%.  $k_2$  is an averaged energy release rate, representing multiple chemical reactions whose yield improves with pressure increase. The nonmonotonic behavior of  $k_1$  when density is varied can be understood based on the transition between the lower pressure initial decomposition mechanism, unimolecular C–N bond break, and the higher pressure initial route (around CJ state), CH<sub>3</sub>NO production. The rate of the former unimolecular reaction is suppressed by pressure rise due to

collisions, whereas the rate of the bimolecular (or higher) reactions forming  $\text{CH}_3\text{NO}$  increases with pressure.

The activation energies extracted in the initial and intermediate stages of NM decomposition are  $E_{a1} = 49.4 \pm 1.3$  kcal/mol (C–N bond break energy, for compression <30%) and  $E_{a2} = 37.5 \pm 3.6$  kcal/mol (an effective value for multiple reactions). The activation energy  $E_{a1}$  for compression  $\geq 30\%$  increases with density due to competing reactions involving  $\text{CH}_3\text{NO}$  production.

The calculated enthalpy change for hot NM decomposition at ambient liquid density is in a very good agreement (<3% deviation) with the measured value.<sup>22</sup> Starting from ambient density,  $\Delta H$  increases until it reaches a peak between 20 and 30% compression; thereafter it begins to decrease when compression increases. This variation of  $\Delta H$  with density might be related to the initial decomposition path of NM: C–N bond break at low densities versus  $\text{CH}_3\text{NO}$  fragment formation at higher compressions. The observed correlation between  $\Delta H$  and initial reaction needs to be further explored for other materials. If this is shown to be a general behavior, the high sensitivity of  $\Delta H$  to the decomposition mechanism, together with its straightforward extraction from simulations, makes it a convenient and useful global parameter for detecting reaction dynamics under various conditions.

Final gaseous fragments asymptotic amounts were calculated. A very good agreement between the measured and calculated amounts was obtained. Both in measurement and simulation,  $\text{H}_2\text{O}$  was found to be the most abundant molecule.

It was shown that atomic ALDCs are more sensitive to the reactions dynamics than the monotonous MSD curves, and can be used to distinguish between time periods where chemical reactions occur and time periods that are diffusion-dominated and nonreactive. The hydrogen average local diffusion coefficient is more sensitive to reaction dynamics than heavier atoms.

Simulations of the various chemical paths in HE decomposition as a function of density and temperature provide detailed insight and understanding that may enable controlling initiation and propagation of detonation waves in HE materials.

## ■ ASSOCIATED CONTENT

Supporting Information. Cut off parameters in fragments analysis using “BondFrag” code and potential parameters used in ReaxFF. This material is available free of charge via the Internet at <http://pubs.acs.org>.

## ■ ACKNOWLEDGMENT

S.V.Z. and W.A.G. were supported by ARO (MURI-W911NF-05-1-0345) and ONR (N00014-05-1-0778, N00014-09-1-0634). Simulations were performed at DOD Major Shared Resource Centers under a DoD/HPCMP Challenge award (ARON27203C3K). R.K. and Y.Z. acknowledge support of The Center of Excellence for Explosives Detection, Mitigation and Response, Department of Homeland Security.

## ■ REFERENCES

- (1) Shaw, R.; Decarli, P. S.; Ross, D. S.; Lee, E. L.; Stromberg, H. D. *Combust. Flame* **1979**, *35*, 237.
- (2) Rice, S. F.; Foltz, M. F. *Combust. Flame* **1991**, *87*, 109.
- (3) Citroni, M.; Bini, R.; Pagliai, M.; Cardini, G.; Schettino, V. *J. Phys. Chem. B* **2010**, *114*, 9420.

- (4) Hardesty, D. R. *Combust. Flame* **1976**, *27*, 229.
- (5) Piermarini, G. J.; Block, S.; Miller, P. J. *J. Phys. Chem.* **1989**, *93*, 462.
- (6) Bourasseau, E.; Dubois, V.; Desbiens, N.; Maillet, J. B. *J. Chem. Phys.* **2007**, *127*, 084513.
- (7) Hervouet, A.; Desbiens, N.; Bourasseau, E.; Maillet, J. B. *J. Phys. Chem. B* **2008**, *112*, 5070.
- (8) Manaa, M. R.; Reed, E. J.; Fried, L. E.; Galli, G.; Gygi, F. *J. Chem. Phys.* **2004**, *120*, 10146.
- (9) Han, S. P.; Strachan, A.; van Duin, A. C. T.; Goddard, W. A. *J. Phys. Chem. A* **2011** in press.
- (10) Melius, C. F. *J. Phys. IV* **1995**, C4–535.
- (11) For example, Asatryan, R.; Bozzelli, J. W.; Simmie, J. M. *J. Phys. Chem. A* **2008**, *112*, 3172.
- (12) van Duin, A. C. T.; Dasgupta, S.; Lorant, F.; Goddard, W. A. *J. Phys. Chem. A* **2001**, *105*, 9396.
- (13) van Duin, A. C. T.; Strachan, A.; Stewman, S.; Zhang, Q. S.; Xu, X.; Goddard, W. A. *J. Phys. Chem. A* **2003**, *107*, 3803.
- (14) Mueller, J. E.; van Duin, A. C. T.; Goddard, W. A. *J. Phys. Chem. C* **2010**, *114*, 4939.
- (15) Chenoweth, K.; van Duin, A. C. T.; Dasgupta, S.; Goddard, W. A. *J. Phys. Chem. A* **2009**, *113*, 1740.
- (16) Strachan, A.; Kober, E. M.; van Duin, A. C. T.; Oxgaard, J.; Goddard, W. A. *J. Chem. Phys.* **2005**, *122*, 054502.
- (17) Nomura, K.; Kalia, R. K.; Nakano, A.; Vashishta, P.; van Duin, A. C. T.; Goddard, W. A. *Phys. Rev. Lett.* **2007**, *99*, 148303.
- (18) van Duin, A. C. T.; Zeiri, Y.; Dubnikova, Y. F.; Kosloff, R.; Goddard, W. A. *J. Am. Chem. Soc.* **2005**, *127*, 11053.
- (19) Zybin, S. V.; Goddard, W. A.; Xu, P.; van Duin, A. C. T.; Thompson, A. P. *Appl. Phys. Lett.* **2010**, *96*, 081918.
- (20) Zhang, L.; Zybin, S. V.; van Duin, A. C. T.; Dasgupta, S.; Goddard, W. A.; Kober, E. M. *J. Phys. Chem. A* **2009**, *113*, 10619.
- (21) Mochalova, V. M.; Torunov, S. I.; Utikin, A. V.; Garanin, V. A. 14<sup>th</sup> International Detonation Symposium, Idaho, April 11–16, 2010.
- (22) Ornellas, D. L. *J. Phys. Chem.* **1968**, *72*, 2390.
- (23) Benson, S. W. *Thermochemical Kinetics*, 2nd ed.; John Wiley: New York, 1976.
- (24) Hu, W. F.; He, T. J.; Chen, D. M.; Liu, F. C. *J. Phys. Chem. A* **2002**, *106*, 7294.
- (25) Tarver, C. M. *Combust. Flame* **1982**, *46*, 157.
- (26) Hobbs, M. L.; Kaneshige, M. J.; Gilbert, D. W.; Marley, S. K.; Todd, S. N. *J. Phys. Chem. A* **2009**, *113*, 10474.

## ■ NOTE ADDED AFTER ASAP PUBLICATION

This article posted ASAP on August 24, 2011. The 8th equation beneath Table 6 on page 10195 has been revised. The correct version posted on September 8, 2011.